


Cite this: *Dalton Trans.*, 2025, **54**, 298

# Development of polyoxometalate-loaded MOFs for heterogeneous catalysis and enhanced dye adsorption†

Ketan Maru, Sarita Kalla and Ritambhara Jangir \*

This study focuses on the enhancement of MIL-117 functionality by incorporating a well-known polyoxometalate (POM), tetrabutylammonium octamolybdate [(*n*-C<sub>4</sub>H<sub>9</sub>)<sub>4</sub>N]<sub>4</sub>[Mo<sub>8</sub>O<sub>26</sub>]. Using an encapsulation method with conventional heating, Mo<sub>8</sub>O<sub>26</sub><sup>4-</sup> anions were for the first time successfully integrated into MIL-117 tubular channels (Mo<sub>8</sub>O<sub>26</sub>@MIL-117). Comprehensive characterization of the material through FTIR, XRD, BET, FE-SEM, EDX, and XPS confirmed the uniform distribution of Mo<sub>8</sub>O<sub>26</sub><sup>4-</sup> within MIL-117 without compromising its structural integrity. The Mo<sub>8</sub>O<sub>26</sub>@MIL-117 composite demonstrates exceptional catalytic performance in oxidative C–N bond formation and Paal–Knorr pyrrole synthesis, achieving high yields under optimized conditions with diverse amine substrates. Characterization and stability assessments confirm Mo<sub>8</sub>O<sub>26</sub>@MIL-117 as a robust and recyclable catalyst, maintaining structural integrity and catalytic activity over multiple cycles, highlighting its potential for sustainable applications in synthetic chemistry. The composite material was also evaluated for its efficacy in dye removal, specifically targeting methylene blue (MB) and Rhodamine B (RHB) from aqueous solutions. Mo<sub>8</sub>O<sub>26</sub>@MIL-117 exhibited superior adsorption capacity for MB compared to MIL-117 alone, demonstrating high efficiency even at elevated concentrations. The composite showed improved selectivity towards MB over RHB, highlighting its potential for selective dye removal in wastewater treatment applications.

Received 17th September 2024,  
Accepted 4th November 2024

DOI: 10.1039/d4dt02645d

rsc.li/dalton

## 1. Introduction

Metal–organic frameworks (MOFs) are crystalline porous materials defined by metal ions or clusters connected to bi- or multipodal organic linkers.<sup>1,2</sup> Their large surface areas, low framework densities, and high pore volumes make them attractive for various applications, such as gas storage,<sup>3</sup> wastewater treatment,<sup>4</sup> and heterogeneous catalysis.<sup>5,6</sup> The externally accessible nanosized cavities and channels within MOFs facilitate the incorporation of substrates, enhancing their catalytic action.<sup>7,8</sup> Despite the discovery of over 10 000 MOF structures, relatively few studies focus on functionalizing MOFs by incorporating metal ions, organic–inorganic molecules through host–guest interactions (doping), or nanoparticles.<sup>9–11</sup>

Polyoxometalates (POMs) are clusters of anionic metal oxides primarily consisting of high-valent early transition-metal ions interconnected by oxygen atoms.<sup>12–14</sup> Their

modular composition and variable size result in a wide range of POM structures.<sup>15</sup> Due to their versatile acid–base and redox properties, along with their strong abilities for electrostatic interactions, hydrogen bonding, and van der Waals forces, POMs have been found suitable for numerous applications in chemical catalysis and wastewater treatment.<sup>16,17</sup> More specifically, these applications include catalytic oxidation,<sup>18</sup> water oxidation,<sup>19</sup> alkene epoxidation,<sup>20</sup> and phosphodiester hydrolysis,<sup>21</sup> and serving as adsorbents for both cationic and anionic dyes.<sup>22</sup> However, the practical use of POMs in catalytic systems is often limited by their high solubility, low specific surface area, and poor stability under catalytic conditions.<sup>23,24</sup> Additionally, their chemical and thermal instability, as well as their poor stability in water, make them unsuitable for dye removal applications.<sup>25</sup> To address these challenges, various supports have been explored to anchor POMs and create hybrid heterogeneous materials.<sup>26</sup> These supports include mesoporous silica,<sup>27</sup> polymers,<sup>28</sup> covalent organic frameworks (COFs),<sup>29,30</sup> and MOFs.<sup>31,32</sup> The tunability, porosity, and thermal and chemical stability, along with water stability, of MOFs make them appropriate as heterogeneous catalysts, supports for anchored homogeneous catalysts, and dye adsorbents.<sup>33,34</sup> Two main techniques for incorporating POMs into MOFs, known as POM@MOF, are impregnation and encapsulation (Fig. S1†).<sup>35,36</sup> Immobilizing POMs onto MOF

Sardar Vallabhbhai National Institute of Technology, Ichchanath, Surat-395 007, Gujarat, India. E-mail: ritambhara.jangir@chem.svniit.ac.in

† Electronic supplementary information (ESI) available: Optimization of the reaction parameters of the catalytic reactions, tabulated comparison of the heterogeneous catalytic activity of Mo<sub>8</sub>O<sub>26</sub>@MIL-117 with other catalysts, PXRD pattern of MIL-117, reusability UV graph, and NMR spectrum (PDF). See DOI: <https://doi.org/10.1039/d4dt02645d>

supports enhances their stability and reusability in catalytic processes and improves their effectiveness as dye adsorbents.<sup>37</sup> This enhances their performance and expands their practical application across a wider range of chemical reactions and wastewater treatment.<sup>38</sup>

The first POM@MOF was synthesised by Férey and colleagues using the impregnation method where MIL-101 was chosen due to its larger apertures and mesopores.<sup>39</sup> The impregnation method involves directly adding a synthesized POM to a MOF, which requires the MOF to have large apertures to allow POM diffusion.<sup>40</sup> On the other hand, the encapsulation method, which is also known as the “bottle around the ship” method, involves constructing a MOF in the presence of a POM.<sup>41</sup> This technique has been used effectively for MOFs like HKUST-1<sup>42</sup> and other Cu-BTC frameworks (BTC = 1,3,5-benzene-tricarboxylate),<sup>43</sup> the NENU<sup>44</sup> series, MIL-100/101 (Fe, Cr, and Al),<sup>45</sup> and UiO-67.<sup>46</sup> These MOFs have cavities large enough to surround the POM while having apertures of appropriate size that prevent the POM from leaching out. Hatton *et al.* developed an MIL-101/PTA composite and evaluated its catalytic performance across several reactions. This composite showed remarkable efficiency in the Baeyer condensation of benzaldehyde and 2-naphthol, in three-component condensation involving benzaldehyde, 2-naphthol, and acetamide, and in the epoxidation of caryophyllene using hydrogen peroxide. Under microwave-assisted heating, the MIL-101/PTA composites achieved impressive reactant conversion rates, exceeding 80–90%.<sup>47</sup> Recently, Kortz *et al.* successfully synthesized a Pd<sub>13</sub>Se<sub>8</sub>@MIL-101 composite material. This innovative composite was evaluated and demonstrated to be an effective, stable, and recyclable heterogeneous pre-catalyst for the Suzuki–Miyaura cross-coupling reaction. The catalytic reaction proceeded efficiently at room temperature, using eco-friendly solvents such as water and methanol.<sup>48</sup>

Here, we explore the functional applications of MOFs modified by doping with inorganic guest molecules, specifically highlighting MIL-117. MIL-117 stands out due to its strong thermal and chemical stability, along with its spacious tubular channels (~12 Å) that facilitate efficient mass transport.<sup>49</sup> The large tubular channels within MIL-117 also facilitate functionalization with POM anions, enabling the resulting composite materials to be highly effective for various applications. A well-known POM precursor, *i.e.*, tetrabutylammonium octamolybdate  $[(n\text{-C}_4\text{H}_9)_4\text{N}]_4[\text{Mo}_8\text{O}_{26}]$ , has been incorporated which is known as a potent oxidizing agent with good thermal stability in the solid state. The POM@MOF composite, *i.e.*, Mo<sub>8</sub>O<sub>26</sub>@MIL-117, has been developed using the encapsulation method in a round bottom flask (RBF) and conventional heating. A complete characterization study confirms the successful synthesis and encapsulation of Mo<sub>8</sub>O<sub>26</sub><sup>4-</sup> anions within the MIL-117 tubular channels. These comprehensive findings underscore that the Mo<sub>8</sub>O<sub>26</sub><sup>4-</sup> anions are tightly encapsulated within the MIL-117 channels, enhancing the composite's stability and preventing leaching. The Mo<sub>8</sub>O<sub>26</sub>@MIL-117 composite exhibits superior catalytic performance in key reactions, including C–N bond formation

(aldehydes and amines (1° and 2°)) and pyrrole synthesis (2,5-hexadione and amines), highlighting its versatility and potential for advanced catalytic applications in chemical processes. This composite material was also tested for the adsorption of methylene blue (MB) and Rhodamine B (RHB), and it demonstrated a strong affinity towards MB in the MB/RHB mixture, showing selective dye adsorption.

## 2. Results and discussion

### 2.1 Synthesis and characterization of Mo<sub>8</sub>O<sub>26</sub>@MIL-117

Traditionally, the synthesis of MIL-117 involves the hydrothermal method.<sup>49</sup> The Mo<sub>8</sub>O<sub>26</sub>@MIL-117 composite was developed using a standard heating and stirring process conducted in an RBF. As part of the synthesis strategy, both the direct sonication (or impregnation) technique and the *in situ* addition method, also referred to as the “bottle around the ship” or encapsulation method, were employed (Fig. 1 and Fig. S2†). ICP-OES results indicate that the impregnation method achieves only 0.005% Mo loading. In contrast, the encapsulation method, using 1 mmol of  $[(n\text{-C}_4\text{H}_9)_4\text{N}]_4[\text{Mo}_8\text{O}_{26}]$ , results in 1.8% Mo loading, and using 2 mmol leads to 4.4% Mo loading within the tubular cavities of MIL-117 (Table S1†). These results suggest that the encapsulation method is more effective and efficient for trapping Mo<sub>8</sub>O<sub>26</sub><sup>4-</sup> anions in the tubular channels of MIL-117. Furthermore, during the post-synthesis process, washing Mo<sub>8</sub>O<sub>26</sub>@MIL-117 with CH<sub>3</sub>CN and DMF confirms the removal of excess and un-trapped  $[(n\text{-C}_4\text{H}_9)_4\text{N}]_4[\text{Mo}_8\text{O}_{26}]$ , as this compound is highly soluble in these solvents.

The MIL-117 structure features tubular channels with a diameter of 1.2 nm, as reported in the literature (Fig. 2(A)).<sup>49</sup> These channels are quite long due to the overall structure of the MOF and can accommodate Mo<sub>8</sub>O<sub>26</sub><sup>4-</sup> anions (Fig. 2(B)). The Mo<sub>8</sub>O<sub>26</sub><sup>4-</sup> anions measure 0.9 nm in length and 0.6 nm in width, making them a suitable fit for the tubular channels (Fig. 2(C)).<sup>50</sup> Thus, the tubular channels in MIL-117 allow the encapsulation of Mo<sub>8</sub>O<sub>26</sub><sup>4-</sup> anions. The physical confinement enhances stability and prevents the POM anions from leaching out of the MOF. Even in the absence of strong electrostatic or coordination bonds, anions can be held within the channels through van der Waals forces. This is particularly relevant in this case because the channels match the POM dimensions well, ensuring close packing and maximizing these weak interactions. Additionally, the oxygen atoms from Mo<sub>8</sub>O<sub>26</sub><sup>4-</sup> can interact with the indium atoms in MIL-117. Such interactions help in stabilizing the POMs within the channels. The interaction between the MIL-117 tubular channels and Mo<sub>8</sub>O<sub>26</sub><sup>4-</sup> anions is multifaceted and may involve electrostatic interactions, coordination chemistry, hydrogen bonding, van der Waals forces, and physical confinement.

The Fourier transform infrared (FTIR) data of the Mo<sub>8</sub>O<sub>26</sub>@MIL-117 material provide valuable insights into the stretching modes present in its structure. The spectra of Mo<sub>8</sub>O<sub>26</sub>@MIL-117 at different Mo<sub>8</sub>O<sub>26</sub><sup>4-</sup> loadings (1 mmol and

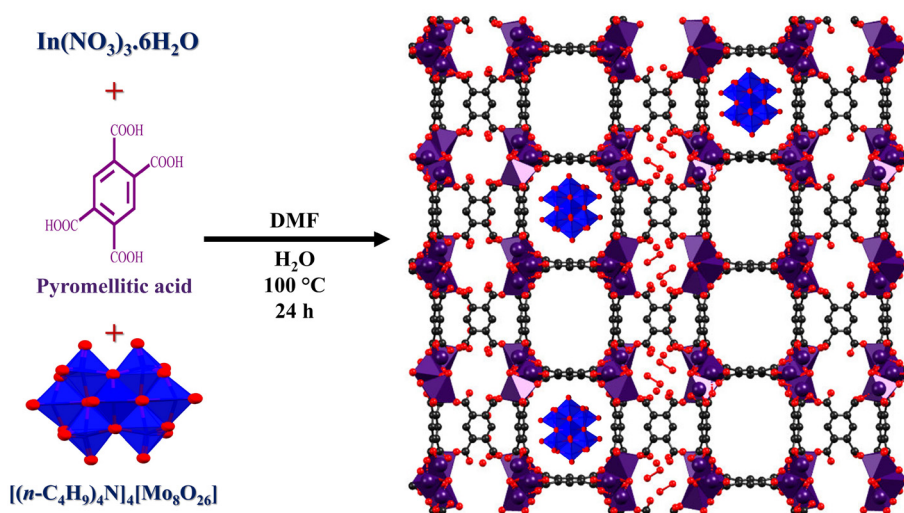


Fig. 1 Synthesis of  $\text{Mo}_8\text{O}_{26}@$ MIL-117 via the encapsulation method utilizing conventional stirring and heating, and proposed structure of the  $\text{Mo}_8\text{O}_{26}@$ MIL-117 composite (grey: carbon, red: oxygen, purple: indium, and blue: Mo, and the image was created using the .cif file from ref. 49).

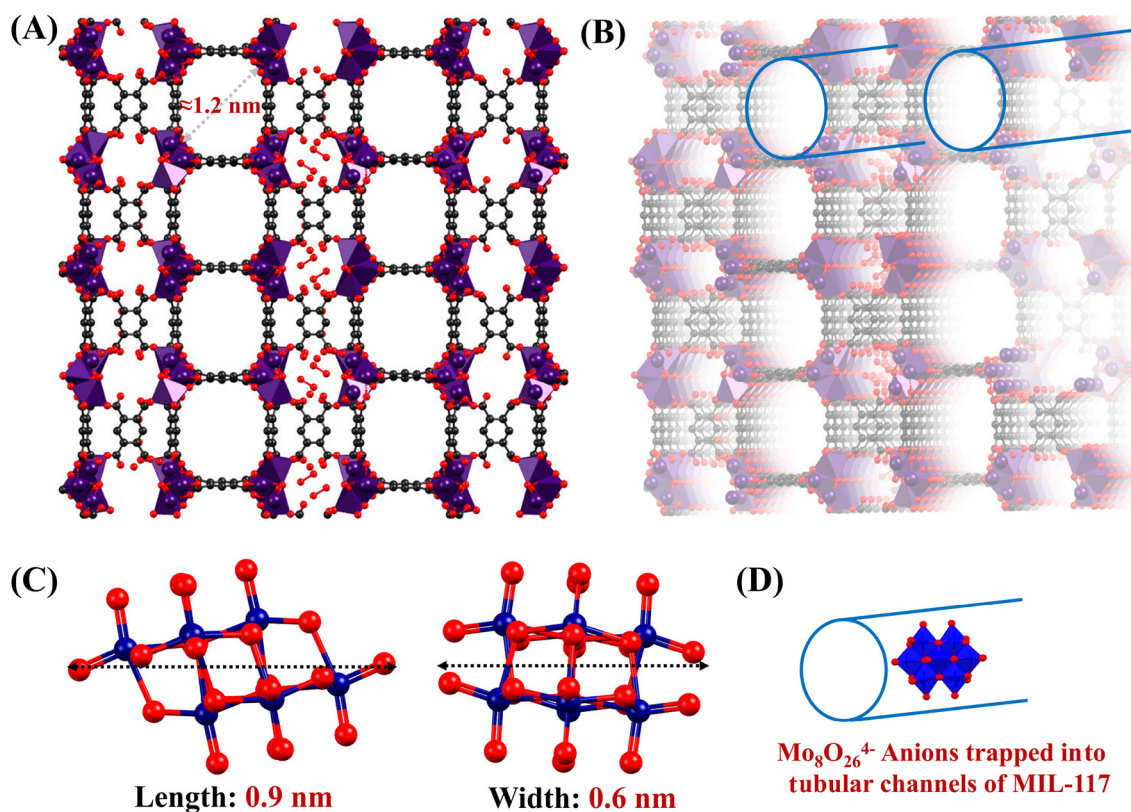


Fig. 2 (A and B) Crystal structure of MIL-117 highlighting its tubular channels with a diameter of 1.2 nm (grey: carbon, red: oxygen, purple: indium, and blue: Mo). (C) Structural views of the  $\text{Mo}_8\text{O}_{26}^{4-}$  anion depicting its X-axis and Y-axis orientations (red: oxygen and blue: Mo) (D). Visual depiction of  $\text{Mo}_8\text{O}_{26}^{4-}$  confined within the tubular channels of MIL-117 (red: oxygen and blue: Mo and the image was created using the .cif file from ref. 49).

2 mmol) exhibit almost similar peak positions. Specifically, the characteristic peaks of the carboxylate group in the MOF are observed at  $1573 \text{ cm}^{-1}$  and  $1583 \text{ cm}^{-1}$  (Fig. 3). Interestingly, the spectra do not show the carboxylic acid

$\nu\text{C}=\text{O}$  peak of the ligand, which typically appears at  $1710 \text{ cm}^{-1}$ . This absence is likely attributed to the formation of carboxylate anions, leading to the establishment of a delocalized electronic cloud and the manifestation of typical carboxy-



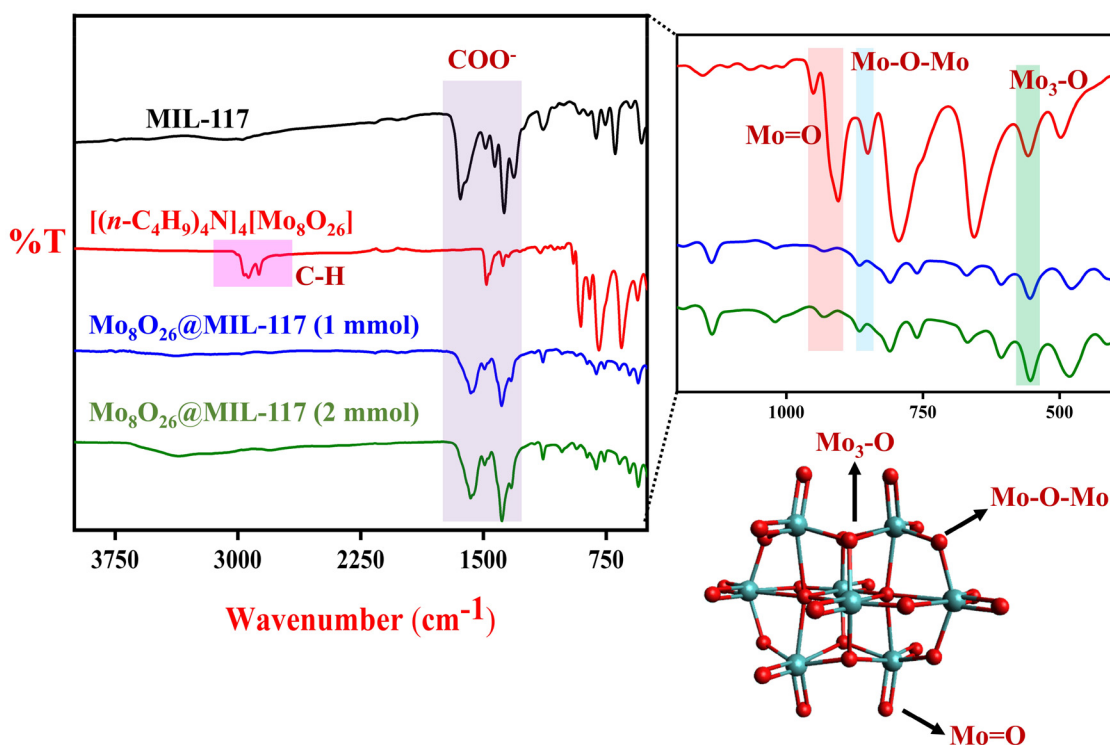


Fig. 3 FTIR spectra of the  $\text{Mo}_8\text{O}_{26}@MIL-117$  composite and  $[(n-C_4H_9)_4N]_4[Mo_8O_{26}]$  (red: oxygen and blue: Mo).

late peaks in the range of  $1610$  to  $1550\text{ cm}^{-1}$  and  $1420$  to  $1300\text{ cm}^{-1}$ . The MIL-117 parent moiety exhibits similar behaviour in its FTIR spectrum. Furthermore, peaks below  $730\text{ cm}^{-1}$ , observed in both  $\text{Mo}_8\text{O}_{26}@MIL-117$  and MIL-117 spectra, suggest the presence of In-O bonding. In the  $500$ – $1000\text{ cm}^{-1}$  region, the observed bands are attributed to the Mo-O stretching modes. The absorption bands at  $909\text{ cm}^{-1}$  and  $912\text{ cm}^{-1}$  are associated with the stretching vibration of Mo=O groups. These peaks appear slightly higher in frequency compared to the parent moiety  $[(n-C_4H_9)_4N]_4[Mo_8O_{26}]$ , which exhibits a peak at  $906\text{ cm}^{-1}$ . The absorption bands at  $851\text{ cm}^{-1}$  in  $[(n-C_4H_9)_4N]_4[Mo_8O_{26}]$  and  $866\text{ cm}^{-1}$  and  $868\text{ cm}^{-1}$  in  $\text{Mo}_8\text{O}_{26}@MIL-117$  correspond to the stretching mode of doubly coordinated oxygen ( $\text{Mo}_2\text{-O}$ ). This mode arises from the oxygen atoms shared between two  $\text{MoO}_6$  octahedra. Additionally, the bands at  $557\text{ cm}^{-1}$  in  $[(n-C_4H_9)_4N]_4[Mo_8O_{26}]$  and  $555\text{ cm}^{-1}$  in  $\text{Mo}_8\text{O}_{26}@MIL-117$  correspond to the stretching mode of triply coordinated oxygen ( $\text{Mo}_3\text{-O}$ ), resulting from the oxygen atoms shared between three  $\text{MoO}_6$  octahedra. The C-H stretching peaks at  $2900\text{ cm}^{-1}$  in  $[(n-C_4H_9)_4N]_4[Mo_8O_{26}]$  are attributed to the tetrabutyl group of this compound. However, in  $\text{Mo}_8\text{O}_{26}@MIL-117$  (1 and 2 mmol), these C-H stretching vibrations are not observed. This absence confirms that the tubular channels of MIL-117 selectively trap the  $\text{Mo}_8\text{O}_{26}^{4-}$  anions, while the  $[(n-C_4H_9)_4N]_4^+$  cations are washed away. These findings confirm that  $\text{Mo}_8\text{O}_{26}^{4-}$  is trapped within the MIL-117 structure, akin to a “ship in a bottle” analogy, where the  $\text{Mo}_8\text{O}_{26}^{4-}$  species is effectively incorporated and immobilized within MIL-117 tubular channels.

The PXRD patterns were recorded to investigate the phase and crystalline structures of the fabricated  $\text{Mo}_8\text{O}_{26}@MIL-117$  sample, as elucidated in Fig. 4(a). In agreement with the simulated pattern with MIL-117, the PXRD patterns of  $\text{Mo}_8\text{O}_{26}@MIL-117$  demonstrate the normal characterization peaks of MIL-117 at  $7.9^\circ$  and  $9.2^\circ$  with high intensity, indicating the good crystallinity of the synthesized  $\text{Mo}_8\text{O}_{26}@MIL-117$ . The prominent peaks observed at  $7.9^\circ$ ,  $9.2^\circ$ ,  $11.4^\circ$ ,  $12.4^\circ$ ,  $16.0^\circ$ ,  $18.7^\circ$ ,  $21.5^\circ$ , and  $24.5^\circ$  correspond to the (020), (004), (110), (024), (041), (008), (144), and (230) planes of MIL-117, which were also found in the synthesized composite (Fig. 4(a)). The main diffraction peaks of  $[(n-C_4H_9)_4N]_4[Mo_8O_{26}]$  are observed at  $2\theta$  of  $8.3^\circ$ ,  $9.9^\circ$ ,  $13.5^\circ$ ,  $15.5^\circ$ ,  $17.9^\circ$ , and  $21.4^\circ$  (Fig. 4(b)). The existence of these diffraction bands attributed to the POM anions in the  $\text{Mo}_8\text{O}_{26}@MIL-117$  pattern, though with very low intensities, indicates the homogeneous distribution of the POM anions in the porous structure of MIL-117. However, peaks assigned to the POM in the composite material were hardly observed, possibly due to the low content and high dispersion of POM molecules.

The  $N_2$  desorption/adsorption isotherms of the  $\text{Mo}_8\text{O}_{26}@MIL-117$  material are displayed in Fig. 4(c). Based on the IUPAC classification, the  $N_2$  adsorption-desorption isotherms of these samples reveal type III isotherms with an H3 hysteresis loop, similar to their parent MIL-117. The specific surface area and total pore volume of this material are presented in Table 1.  $\text{Mo}_8\text{O}_{26}@MIL-117$  exhibited a lower surface area and pore volume, compared to MIL-117 (Table 1). This significant difference is attributed to the insertion of

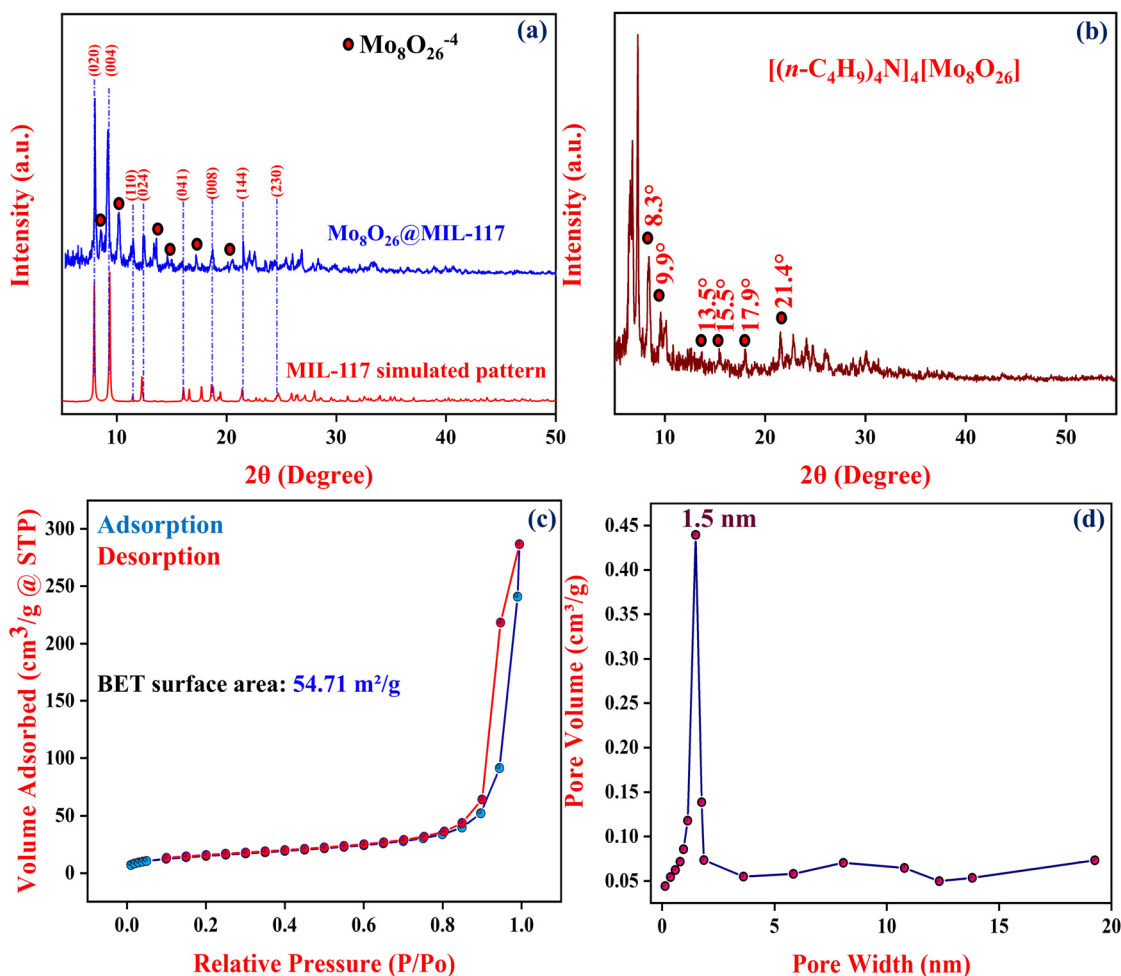


Fig. 4 (a) Comparison of the obtained PXRD patterns of the  $\text{Mo}_8\text{O}_{26}@MIL-117$  composite with the simulated PXRD pattern of MIL-117. (b) PXRD pattern of  $[(n-C_4H_9)_4N]_4[Mo_8O_{26}]$ . (c)  $N_2$  adsorption and desorption isotherm of  $\text{Mo}_8\text{O}_{26}@MIL-117$ . (d) BJH pore size distribution diagram of the  $\text{Mo}_8\text{O}_{26}@MIL-117$  composite.

**Table 1** The surface parameters of MIL-117 and  $\text{Mo}_8\text{O}_{26}@MIL-117$  samples

Samples	BET surface area ( $\text{m}^2 \text{g}^{-1}$ )	Total pore volume ( $\text{cm}^3 \text{g}^{-1}$ )
MIL-117	63 $\text{m}^2 \text{g}^{-1}$	0.77
$\text{Mo}_8\text{O}_{26}@MIL-117$	54.71 $\text{m}^2 \text{g}^{-1}$	0.44

POM anions into the pores of MIL-117, which occupy most of the pore space.

Furthermore, the morphology of the composite material was investigated using FE-SEM analysis, as illustrated in Fig. 5. Pristine MIL-117 particles exhibit an orderly plate-like morphology. However, comparing the FE-SEM images of  $\text{Mo}_8\text{O}_{26}@MIL-117$  with those of MIL-117 shows no specific morphology of MIL-117, indicating that the presence of the POM alters the formation mechanism. The SEM images reveal that  $\text{Mo}_8\text{O}_{26}@MIL-117$  exhibits a flower-like morphology, which is significantly different from its parent compound,

MIL-117 (Fig. 4). Despite this morphological change, the PXRD, BET, and FT-IR results confirm that the framework of MIL-117 did not collapse or degrade after encapsulation with  $\text{Mo}_8\text{O}_{26}^{4-}$  anions. This change in the morphology is attributed to the encapsulation of  $\text{Mo}_8\text{O}_{26}^{4-}$  anions within the MOF channels. These anions are tightly trapped, causing some distortion in the structure. This structural distortion, along with the interpenetration of anions into the channels, leads to the observed morphological changes. To further investigate the distribution and chemical composition of the  $\text{Mo}_8\text{O}_{26}@MIL-117$  composite, EDX elemental mapping was performed (Fig. 5(c)). A representative SEM image with the corresponding EDX elemental mappings in Fig. 5(c) shows the uniform distribution of C, O, In, and Mo elements in the flower-like  $\text{Mo}_8\text{O}_{26}@MIL-117$  particles, emphasizing the homogeneity of the prepared sample.

X-ray photoelectron spectroscopy (XPS) analysis was conducted on  $\text{Mo}_8\text{O}_{26}@MIL-117$  to provide a detailed understanding of the bonding interactions. The results, presented in Fig. 6, provide significant insights into the chemical states and

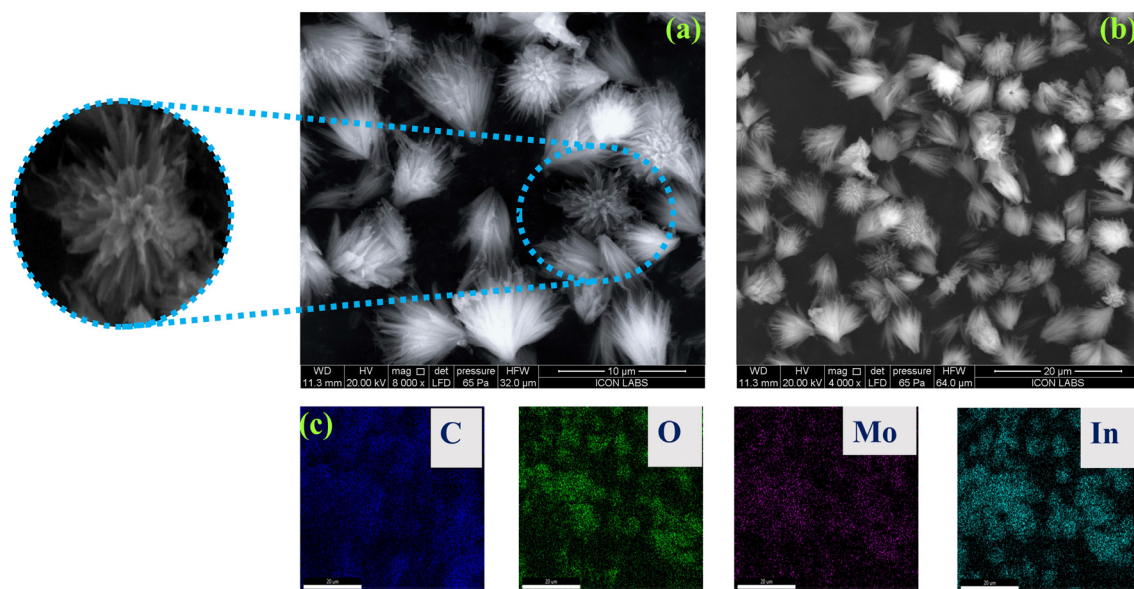


Fig. 5 (a and b) SEM images of  $\text{Mo}_8\text{O}_{26}$ @MIL-117 and (c) EDS mapping of the  $\text{Mo}_8\text{O}_{26}$ @MIL-117 composite.

bonding environment of the elements within the composite. Notable peaks were observed at specific binding energies (BEs), including 285 eV (C 1s), 530 eV (O 1s), 443 eV (In 3d), and 232 eV (Mo 3d) (Fig. 6a). The C 1s and O 1s elements were identified in the pyromellitic acid linker. The high-resolution C 1s peak exhibited four prominent peaks at 286.3 eV, 287.8 eV, and 288.8 eV BEs, corresponding to C–O, C=O, and O–C=O groups, respectively (Fig. 6b). The O 1s spectra displayed distinct peaks at BEs of 531.5 eV, 532.3 eV, 533.2 eV, and 530.5 eV, which are associated with C=O, C–O, O–C=O, and Mo–O bonds, respectively (Fig. 6c). The peaks observed at 232 eV and 235 eV binding energies (BEs) in the XPS analysis further confirm the presence of  $\text{Mo}_8\text{O}_{26}^{4-}$  within the composite (Fig. 6e). The XPS spectra of Mo show identical characteristics to those found in the literature of  $\text{Mo}_8\text{O}_{26}^{4-}$ , confirming that the oxidation state of molybdenum in the composite is the same as that in  $\text{Mo}_8\text{O}_{26}^{4-}$ . This BE is consistent with that of the  $\text{Mo}_8\text{O}_{26}^{4-}$  entity and matches the state found in its parent compound  $[(n\text{-C}_4\text{H}_9)_4\text{N}]_4[\text{Mo}_8\text{O}_{26}]$ . These findings strongly suggest that  $\text{Mo}_8\text{O}_{26}^{4-}$  is indeed trapped within the channels of MIL-117. The characteristic peaks of In were observed at BEs between 443 and 445 eV, specifically at 443.8 eV (In 3d<sub>5/2</sub>) and 445.1 eV (In 3d<sub>3/2</sub>) (Fig. 6d). Additionally, the peak at 445.1 eV confirmed that In is surrounded by oxygen atoms from the pyromellitic acid linker, like tris(2,4-pentanedionato-O,O')indium. These XPS results suggest that the MIL-117 structure is formed around  $\text{Mo}_8\text{O}_{26}^{4-}$  like a ship in the bottle.

The thermal behaviour exhibited by  $\text{Mo}_8\text{O}_{26}$ @MIL-117 closely resembles that of MIL-117, as illustrated in Fig. 6f. The similarity observed implies a lack of strong covalent bonding between the MIL-117 and  $\text{Mo}_8\text{O}_{26}^{4-}$  anions. This suggests that the  $\text{Mo}_8\text{O}_{26}^{4-}$  is trapped within the channels and is not part of

the building block of the composite structure, nor is it directly attached to the structure. Instead, the interaction is likely mediated by electrostatic interactions, hydrogen bonding, and van der Waals forces, and physical confinement within the composite structure is possible. However, an increase in the amount of metal oxide residue can be observed in  $\text{Mo}_8\text{O}_{26}$ @MIL-117 (1 mmol: 36% and 2 mmol: 38%), which suggests that the  $\text{Mo}_8\text{O}_{26}^{4-}$  species is effectively trapped inside the MIL-117 structure. The TGA curves of MIL-117 and  $\text{Mo}_8\text{O}_{26}$ @MIL-117 show two major weight losses, and the first weight loss up to 100 °C is attributed to the removal of physisorbed water. The second weight loss, performed in two steps, between 250 °C and 500 °C, indicates the decomposition of the benzenetetracarboxylate ligand and removal of its fragments. The final residue corresponds to a mixture of indium oxide and molybdenum oxide. In comparison,  $[(n\text{-C}_4\text{H}_9)_4\text{N}]_4[\text{Mo}_8\text{O}_{26}]$  remains stable up to 257 °C. At this temperature,  $\text{Mo}_8\text{O}_{26}$ @MIL-117 also begins to degrade, and due to the very low concentration of anions, it becomes challenging to distinguish a clear signature for  $[(n\text{-C}_4\text{H}_9)_4\text{N}]_4[\text{Mo}_8\text{O}_{26}]$  within the composite. This overlap in degradation behavior suggests that the presence of the anions does not significantly alter the thermal profile of the composite.

In conclusion, the FTIR data confirm the presence of  $\text{Mo}_8\text{O}_{26}^{4-}$  in its original form. PXRD analysis indicates that the structure or channels did not collapse and that the material maintained good crystallinity. BET measurements show that the channels are filled, leading to a reduced surface area. Additionally, XPS data confirm that the oxidation state of Mo remains unchanged from its parent moiety. These combined results confirm that MIL-117 successfully traps  $\text{Mo}_8\text{O}_{26}^{4-}$  anions within its hollow channels without any structural degradation.

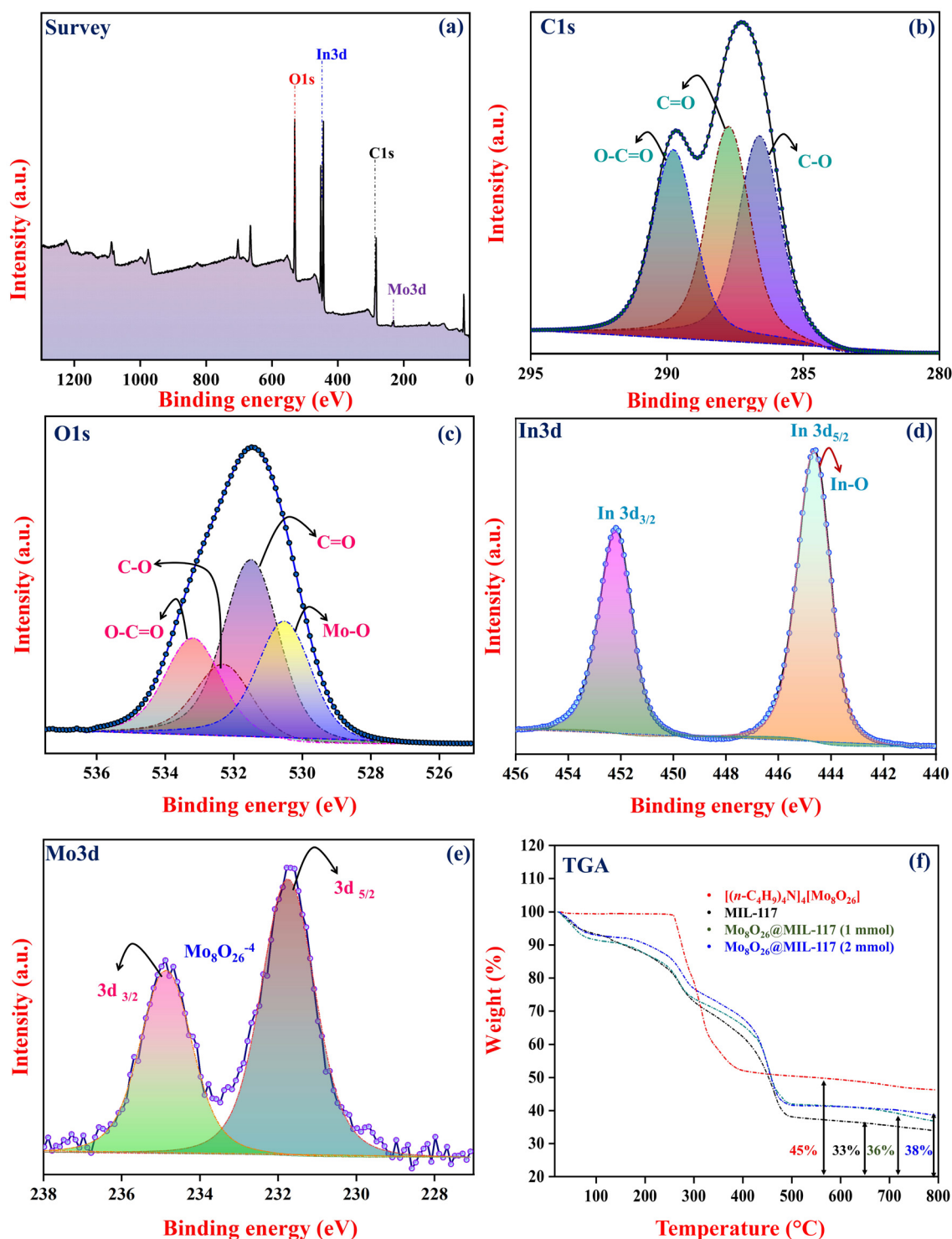


Fig. 6 (a) XPS spectra survey scan of the prepared  $\text{Mo}_8\text{O}_{26}@MIL-117$ . (b–e) High-resolution C 1s, O 1s In 3d and Mo 3d XPS spectra of  $\text{Mo}_8\text{O}_{26}@MIL-117$ . (f) TG curves of MIL-117,  $[(n-C_4H_9)_4N]_4[Mo_8O_{26}]$  and  $\text{Mo}_8\text{O}_{26}@MIL-117$  under a  $N_2$  atmosphere.

## 2.2 Catalytic study

The synthesis of the  $\text{Mo}_8\text{O}_{26}@MIL-117$  composite material represents a significant leap in catalysis, as it demonstrates remarkable efficacy in two pivotal reactions: C–N bond for-

mation using primary and secondary amines and Pall Knorr pyrrole synthesis. Harnessing the synergistic properties of MIL-117 and  $\text{Mo}_8\text{O}_{26}^{4-}$ , this composite catalyst exhibits exceptional versatility. Its ability to catalyse oxidative C–N bond formation highlights its role in enabling crucial synthetic path-



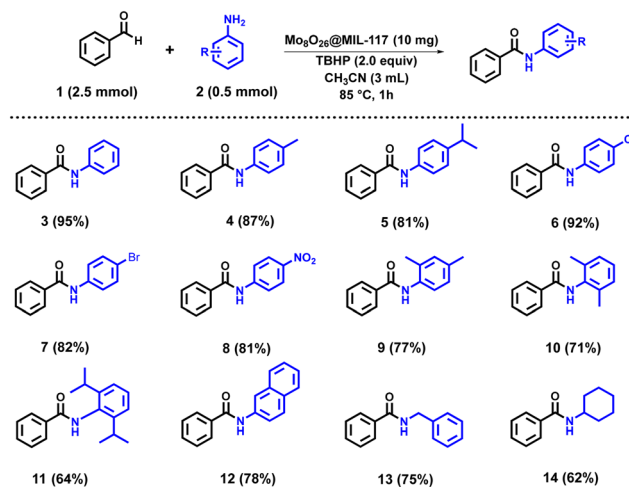
ways. At the same time, its effectiveness in pyrrole synthesis underscores its relevance in producing valuable compounds that have diverse applications in pharmaceuticals and materials science. This multifunctional catalyst showcases promising potential for broadening synthetic possibilities and advancing catalytic methodologies.

**2.2.1 Oxidative C–N bond formation.** Amide bonds are fundamental in natural products, polymers, and pharmaceuticals; hence, the formation of these bonds is historically rooted in classical organic transformations, primarily involving reactions of amines with carboxylic acids and their derivatives using famous processes like the Schmidt and Beckmann rearrangements. Among new methods, direct cross-dehydrogenative coupling (CDC) of aldehydes with amines has emerged as a promising approach. In the present study of oxidative C–N bond formation *via* CDC of benzaldehyde with amines (1° and 2°), the synthesized  $\text{Mo}_8\text{O}_{26}@MIL-117$  composite was employed as a catalyst. The selection of  $\text{Mo}_8\text{O}_{26}^{4-}$  was strategic due to its potent oxidizing properties, which are essential for facilitating the CDC reactions. Integrating  $\text{Mo}_8\text{O}_{26}^{4-}$  within the MIL-117 framework enhances its catalytic efficiency and provides a stout and stable platform for the oxidative processes involving the formation of C–N bonds.

In the pursuit of efficient oxidative C–N bond formation, a meticulous optimization process was embarked upon, aiming to enhance both yield and selectivity while elucidating critical reaction parameters. Initially, a model reaction between benzaldehyde (**1**) and aniline (**2**) was selected, employing TBHP (*tert*-butyl hydroperoxide) as the oxidant to synthesize benzamide (**3**) and to identify the most effective catalytic system (Table S2†). The catalyst screening experiment, conducted in acetonitrile at 75 °C for 1 hour, entailed evaluating the  $\text{Mo}_8\text{O}_{26}@MIL-117$  catalyst with 1 mmol and 2 mmol  $\text{Mo}_8\text{O}_{26}^{4-}$  loadings, alongside other catalysts such as MIL-117,  $[(n\text{-C}_4\text{H}_9)_4\text{N}]_4[\text{Mo}_8\text{O}_{26}]$ , and  $\text{In}(\text{NO}_3)_3 \cdot x\text{H}_2\text{O}$ . Remarkably,  $\text{Mo}_8\text{O}_{26}@MIL-117$  (2 mmol) at 10 mg loading exhibited the highest yield of 74%, outperforming the other catalysts and loadings, signifying its superior catalytic activity. The subsequent optimization steps delved into various factors influencing the reaction efficiency. Temperature screening (Table S3†) identified 85 °C as the optimal temperature, maximizing the efficiency of the catalyst. Solvent screening (Table S4†) provided critical insights, with acetonitrile emerging as the optimal solvent, yielding 84% product formation, attributed to its polar aprotic nature facilitating effective solvation of reactants and the oxidant. Further investigation into the reaction time (Table S5†) revealed 60 minutes as the optimal duration, yielding 84% product formation, beyond which prolonged reaction times exhibited diminishing returns, indicative of completion of the reaction. Furthermore, in oxidant screening, TBHP exhibited the highest yield of 84%, attributed to its efficient generation of radical species essential for oxidation. Other oxidants, such as benzoyl peroxide ( $\text{BZ}_2\text{O}_2$ ), yielded a moderate 74%, while di-*tert*-butyl peroxide (DTBP) and dicumyl peroxide (DCP) showed lower reactivity, yielding 54% and 51% of the product, respectively (Table S6†). Additionally,

oxidant loading screening (Table S7†) demonstrated that an oxidant loading of 2.0 equivalents maximized the yield (94%), ensuring a balanced efficiency in oxidant utilization. Substrate ratio screening (Table S8†) further elucidated the significance of stoichiometry, with a ratio of 1 : 5 between the amine and aldehyde providing optimal conditions for maximizing product formation, with yields reaching 95%. Collectively, these optimization endeavours underscore the intricate interplay of various parameters in oxidative C–N bond formation. A systematic exploration of catalysts, temperature, solvent, reaction time, oxidant type and loading, and substrate ratio was undertaken to optimize the reaction conditions. This investigation not only refined the parameters but also provided critical insights into the individual and combined effects of these variables, elucidating the synergistic interaction between MIL-117 and  $[(n\text{-C}_4\text{H}_9)_4\text{N}]_4[\text{Mo}_8\text{O}_{26}]$  in the composite. Notably, this study highlights a significant improvement in the C–N bond formation yield when both components are employed in tandem. While MIL-117 and  $[(n\text{-C}_4\text{H}_9)_4\text{N}]_4[\text{Mo}_8\text{O}_{26}]$  individually achieve yields of 13% and 39%, respectively, their combination in the composite results in a remarkable yield of 95%. This dramatic enhancement underscores the synergistic interaction, demonstrating that the cooperative behavior between MIL-117 and  $[(n\text{-C}_4\text{H}_9)_4\text{N}]_4[\text{Mo}_8\text{O}_{26}]$  significantly boosts catalytic performance, far surpassing the efficacy of either.

After optimizing the model reaction, the substrate scope was explored using a variety of primary aromatic, poly-aromatic, benzyl, and cyclic amines with benzaldehyde under the established conditions. The reaction proved versatile, yielding primary amides (Scheme 1) in good to excellent yields, regardless of the electronic nature of substituents on the aromatic amines. For instance, amines with electron-withdrawing groups (–Cl (**6**), –Br (**7**), and –NO<sub>2</sub> (**8**)) resulted in products in high yields of 92%, 82%, and 81%, respectively, demonstrating the reaction's robustness against different electronic effects.

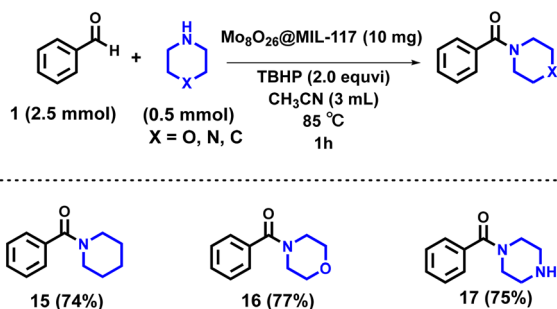


**Scheme 1** Oxidative C–N bond formation with benzaldehyde and primary amines catalysed by  $\text{Mo}_8\text{O}_{26}@MIL-117$  (2 mmol  $\text{Mo}_8\text{O}_{26}^{4-}$  loading). Isolated yield in brackets.



Furthermore, the reaction conditions with the  $\text{Mo}_8\text{O}_{26}@MIL-117$  catalyst performed well with sterically hindered amines. 2,6-Diisopropyl amine (**11**), which features bulky substituents, produced a slightly lower yield (64%) than less sterically hindered substrates due to the increased steric hindrance. Additionally, benzylamine (**13**) and cyclic aliphatic amines, such as cyclohexylamine (**14**), delivered yields of 75% and 62%, respectively, showcasing the catalyst's efficacy with various amine structures. Lastly, the catalytic system efficiently facilitated reactions with polyaromatic amines. Specifically, naphthylamine (**12**) combined with benzaldehyde to yield 78%, demonstrating the catalyst's capability to handle more complex aromatic systems effectively. This underscores the versatility and robustness of the  $\text{Mo}_8\text{O}_{26}@MIL-117$  catalyst in promoting oxidative C–N bond formation across a wide range of substrates.

Furthermore, the  $\text{Mo}_8\text{O}_{26}@MIL-117$  catalyst demonstrated remarkable efficiency not only with primary amines but also with secondary amines. Under the same optimized conditions, secondary amines such as piperidine, morpholine, and piperazine yielded secondary amides in good yields. Specifically, piperidine (**15**) yielded 74%, morpholine (**16**) gave 77%, and piperazine (**17**) achieved a 75% yield. These results indicate the catalyst's versatility and durability across different types of amines, successfully facilitating oxidative C–N bond formation with both primary and secondary amines (Scheme 2). Moreover, when comparing the performance of  $\text{Mo}_8\text{O}_{26}@MIL-117$  to that of other MOFs or MOF-based composites (Table 2), our catalyst consistently shows superior yields



**Scheme 2** Oxidative C–N bond formation with benzaldehyde and secondary amines catalysed by  $\text{Mo}_8\text{O}_{26}@MIL-117$  (2 mmol  $\text{Mo}_8\text{O}_{26}^{4-}$  loading). Isolated yield in brackets.

**Table 2** Some reported MOF-based catalysts used for oxidative C–N bond formation

Entry	MOF or POM@MOF composites	Yield <sup>a</sup> [%]	Time	Recyclable	Ref.
1	Pd/MIL-101(Fe)	94	24 h		51
2	Cu-MOF	75	1 h	Yes	52
3	SiW <sub>9</sub> Ni <sub>6</sub> -DPNDI	88	24 h		53
4	NiO@Ni	98	8 h		54
5	$\text{Mo}_8\text{O}_{26}@MIL-117$	95	1 h	Yes	This work

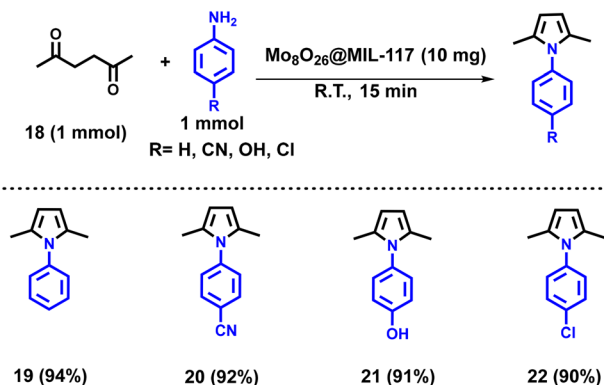
<sup>a</sup> Isolated yield.

in oxidative C–N bond formation. These results highlight the unique catalytic properties of the  $\text{Mo}_8\text{O}_{26}@MIL-117$  composite, making it a highly effective catalyst for useful organic transformations. The potential of the material as a benchmark catalyst for oxidative C–N bond formation reactions offers a stout and versatile solution.

**2.2.2 Paal–Knorr pyrrole synthesis.** The synthesis of nitrogen-containing heterocycles, crucial for various natural products, pharmaceuticals, and materials, has been a significant focus in chemistry.<sup>55</sup> Pyrrole rings, in particular, are vital due to their applications in medicine, materials science, and catalysis.<sup>56</sup> Pyrrole derivatives possess diverse biological activities, such as antitumor, anti-inflammatory, hypolipidemic, and antimicrobial properties.<sup>57</sup> While many methods exist for creating substituted pyrroles, the Paal–Knorr reaction remains the most reliable and efficient method, involving the cyclization of 2,5-hexazinone with aromatic amine compounds to form pyrrole rings.<sup>58</sup> Farahi *et al.* prepared a  $\text{GO}@TiO_2/(\text{CH}_2)_3\text{N}=\text{Mo}[\text{Mo}_5\text{O}_{18}]$  composite, trapping  $\text{Mo}_5\text{O}_{18}^{2-}$  anions, and used it as a nano-catalyst in the Paal–Knorr reaction for pyrrole synthesis. Despite its good catalytic activity, the application of the catalyst is hindered by a complicated, multi-step synthesis process and high costs of preparation.<sup>59</sup> These challenges could be effectively addressed by employing the  $\text{Mo}_8\text{O}_{26}@MIL-117$  catalyst.

Here, we have utilized the  $\text{Mo}_8\text{O}_{26}@MIL-117$  composite material for the Paal–Knorr synthesis. In the quest for optimal synthesis of pyrrole derivatives *via* the Paal–Knorr reaction, a systematic optimization endeavour was undertaken. This rigorous process aimed to elevate yield, while unravelling pivotal reaction parameters essential for fine-tuning the reaction conditions. Catalyst screening (Table S9<sup>†</sup>) revealed that  $\text{Mo}_8\text{O}_{26}@MIL-117$  catalysts, particularly with 2 mmol  $\text{Mo}_8\text{O}_{26}^{4-}$  loading, exhibited superior performance, yielding up to 94% at a loading of 10 mg. Solvent screening (Table S10<sup>†</sup>) highlighted the solvent-free condition as optimal, achieving a remarkable yield of 94%, indicating enhanced efficiency without solvent interference. Time screening (Table S11<sup>†</sup>) further refined the reaction conditions, demonstrating that a reaction time of 15 minutes yielded optimal results with a consistent 94% yield. Substrate ratio screening (Table S12<sup>†</sup>) reinforced the versatility of the reaction, showcasing high yields (93–94%) across various aniline to 2,5-hexadione ratios. These systematic optimization studies provide valuable insights into enhancing the efficiency and reliability of pyrrole synthesis.

After meticulously optimizing the model reaction, an extensive exploration of the substrate scope was conducted, employing various primary aromatic amines alongside 2,5-hexadione under the established conditions (Scheme 3). Notably, the catalyst exhibited exceptional performance across a spectrum of electron-releasing (–OH (**22**)) and electron-withdrawing groups (–CN (**21**) and –Cl (**23**)), yielding 92%, 91%, and 92%, respectively. This comprehensive investigation demonstrated the versatility of the reaction, consistently delivering well to excellent yields irrespective of the electronic properties of the



**Scheme 3** Paal–Knorr synthesis of pyrrole using the  $\text{Mo}_8\text{O}_{26}\text{@MIL-117}$  catalyst.

substituents on the aromatic amines. Furthermore, upon comparing the efficacy of  $\text{Mo}_8\text{O}_{26}\text{@MIL-117}$  with that of other MOFs or MOF-based composites and other composites as

**Table 3** Reported catalysts used for Paal–Knorr pyrrole synthesis

Entry	MOF or POM@MOF composites	Yield <sup>a</sup> [%]	Time (min)	Ref.
1	IRMOF-3	90	60 min	60
2	GO@TiO <sub>2</sub> /(CH <sub>2</sub> ) <sub>3</sub> N=Mo[Mo <sub>5</sub> O <sub>18</sub> ]	96	20 min	59
3	Ru-MOF	48	240 min	61
4	$\text{Mo}_8\text{O}_{26}\text{@MIL-117}$	94	15 min	This work

<sup>a</sup> Isolated yield.

listed in Table 3, our catalyst consistently demonstrates superior performance in Paal–Knorr synthesis, yielding higher product yields. This underscores the exceptional catalytic capabilities of the  $\text{Mo}_8\text{O}_{26}\text{@MIL-117}$  composite, establishing it as a highly efficient catalyst for such transformations in recent investigations.

### 2.3 Catalyst reusability, stability and leaching study

The  $\text{Mo}_8\text{O}_{26}\text{@MIL-117}$  catalyst exhibits exceptional stability and reusability, as evidenced by its performance in amide bond formation reactions. A series of recycling experiments were conducted to assess the catalyst's strength. After each catalytic run, the material was separated by centrifugation, thoroughly washed with ethanol, and dried at 80 °C before being reused in subsequent reactions with fresh substrates. Remarkably, as shown in Fig. 7e, the catalyst consistently achieved high yields of the amide product over four consecutive cycles without any significant decline in catalytic activity. This indicates the durable performance and resilience of the catalyst under the reaction conditions. Further structural analysis of the catalyst was carried out to confirm post-catalysis integrity. PXRD patterns demonstrated that the characteristic peaks of the MIL-117 framework in the  $\text{Mo}_8\text{O}_{26}\text{@MIL-117}$  structure remained largely unchanged after catalysis, as illustrated in Fig. 7b. This finding underscores that the MIL-117 framework maintains its structural integrity even after the catalytic process, indicating the stability of the composite. Additionally, the N<sub>2</sub> adsorption–desorption isotherm revealed a decrease in the surface area of the  $\text{Mo}_8\text{O}_{26}\text{@MIL-117}$  catalyst after the catalytic cycles (Fig. 7a). Despite this reduction, the isothermal behaviour classified by the IUPAC remained con-

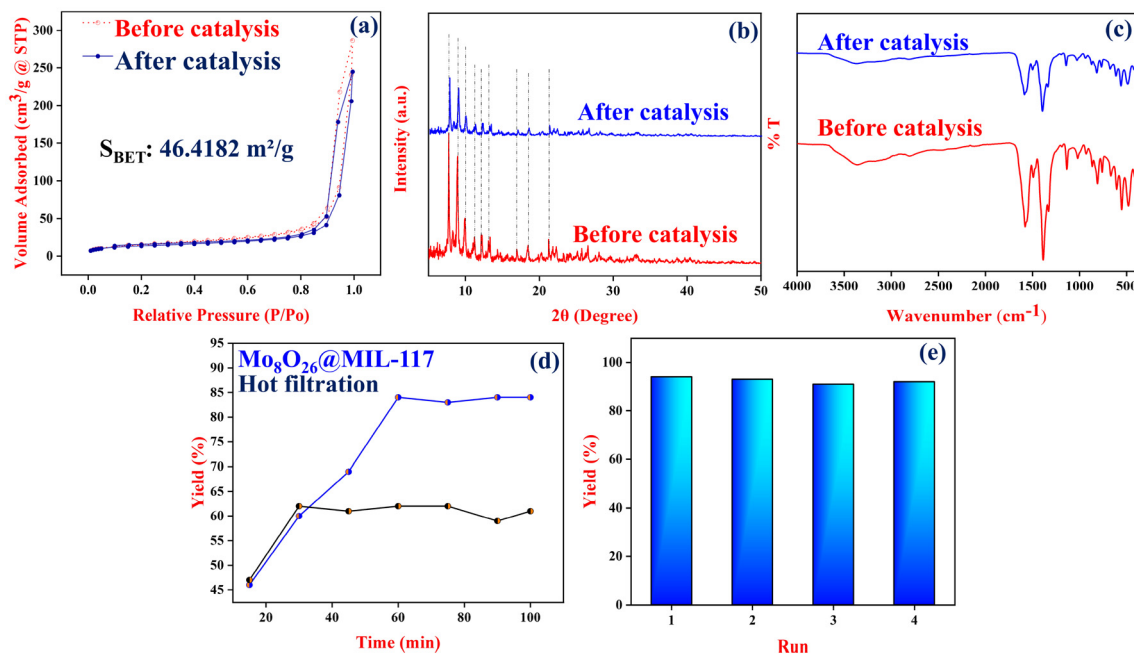


**Fig. 7** (a) The N<sub>2</sub>-adsorption isotherms of fresh  $\text{Mo}_8\text{O}_{26}\text{@MIL-117}$  (red curve) compared to those after (blue curve) catalysis. (b) FT-IR and (c) PXRD of the recovered heterogeneous catalyst after the 4<sup>th</sup> run. (d) Hot filtration test. (e) Catalyst reusability.

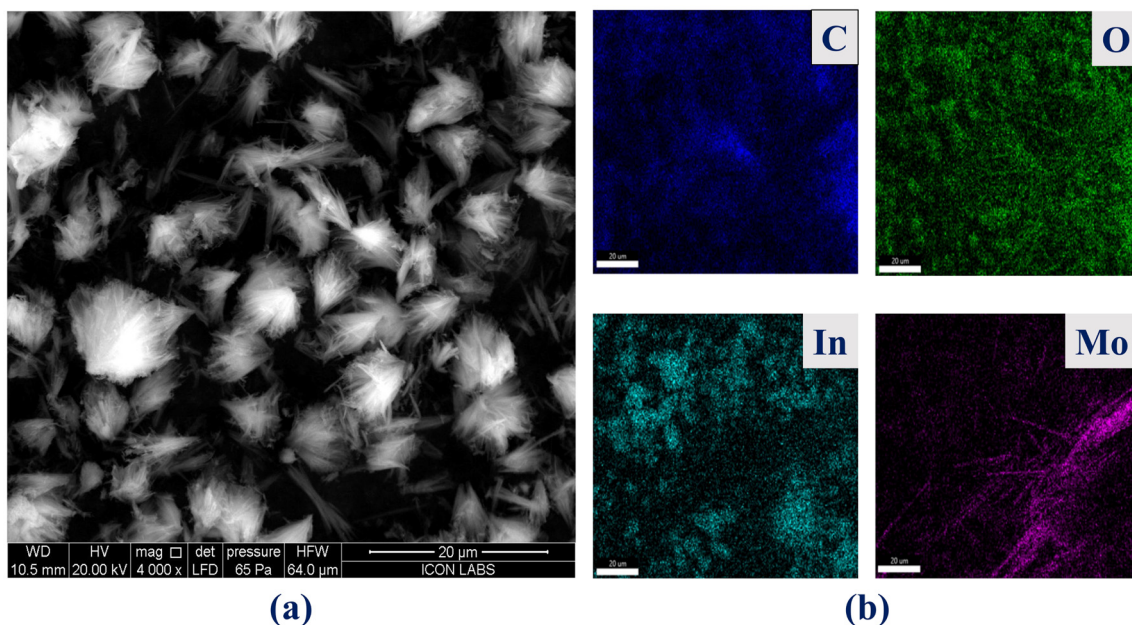


**Fig. 8** (a) High-resolution SEM image of  $\text{Mo}_8\text{O}_{26}@MIL-117$  after four catalytic cycles for oxidative C–N bond formation, highlighting the morphological integrity and surface characteristics. (b) EDX elemental mapping of  $\text{Mo}_8\text{O}_{26}@MIL-117$  after four catalytic cycles for oxidative C–N bond formation, illustrating the spatial distribution and retention of key elements.

sistent with that of the fresh composite material even after the fourth catalytic cycle. This consistency suggests that the tubular channels of the catalyst are preserved, and the overall structure of  $\text{Mo}_8\text{O}_{26}@MIL-117$  does not collapse during the catalytic process. SEM analysis further supported the stability of the catalyst, and SEM images showed that the morphology of the microcrystallites of  $\text{Mo}_8\text{O}_{26}@MIL-117$  remained unchanged post-catalysis (Fig. 8a). This observation corroborates that the catalytic reaction does not impact the physical structure of the composite, maintaining the integrity of both the MIL-117 framework and the overall composite throughout the catalytic process. Fig. 8b displays EDX mapping, revealing the consistent dispersion of essential elements throughout the catalyst after catalysis. FT-IR analysis was performed on the  $\text{Mo}_8\text{O}_{26}@MIL-117$  composite after the fourth cycle to validate the structural stability further. The FT-IR spectra of the used catalyst closely matched those of the fresh catalyst, as depicted in Fig. 7c. In summary, the  $\text{Mo}_8\text{O}_{26}@MIL-117$  catalyst not only demonstrates high catalytic efficiency but also maintains its structural and morphological stability under repeated catalytic cycles. This robust performance makes it a highly effective and reliable catalyst for amide bond formation and potentially other catalytic applications.

To evaluate the potential leaching of  $\text{Mo}_8\text{O}_{26}^{4-}$  from MIL-117 during catalysis, the reaction mixture of amide synthesis with  $\text{Mo}_8\text{O}_{26}@MIL-117$  was filtered after 30 minutes, and the reaction progress was monitored thereafter (Fig. 7d). There was no observable progress in the reaction, suggesting no solid catalyst leakage into the reaction mixture. This confirms the heterogeneous nature of  $\text{Mo}_8\text{O}_{26}@MIL-117$ . Furthermore, post-filtration ICP-OES analysis revealed no mol-

ybdenum presence in the reaction mix (Table S13<sup>†</sup>), indicating effective trapping of  $\text{Mo}_8\text{O}_{26}^{4-}$  within the composite and the preservation of its structural integrity.

#### 2.4 Dye removal

POMs have shown potential in dye removal applications, but their practical utility is often compromised due to several inherent limitations.<sup>62</sup> These include poor water stability, limited surface areas (typically less than  $10 \text{ m}^2 \text{ g}^{-1}$ ), and high solubility in aqueous solutions, which complicate their recycling and reuse.<sup>24</sup> MOFs often face challenges such as poor water stability and pore blockage, which can hinder their effectiveness in dye removal. However, integrating POMs into MOFs to create POM@MOF composites helps to address these issues, resulting in a material with superior dye removal efficiency.<sup>23</sup> This synergy makes POM@MOF composites a potent solution for overcoming the limitations of their components.<sup>24</sup> For instance, while MOFs like MIL-117 are effective in adsorption, their performance can be significantly enhanced when combined with  $\text{Mo}_8\text{O}_{26}^{4-}$ , leading to improved functionality and stability. We investigated the adsorption properties of the  $\text{Mo}_8\text{O}_{26}@MIL-117$  composite and compared its performance to that of the parent MIL-117 framework. Our study specifically focused on the removal of cationic dyes, MB and RHB, from aqueous solutions. The studies also focused on the selective removal efficiency of MB over RHB, providing insights into the composite's preferential adsorption behaviour for these dyes.

For the adsorption experiments, solutions were prepared with MB concentrations varying from 10 to 120 ppm. The adsorbent, either 10 milligrams of MIL-117 or  $\text{Mo}_8\text{O}_{26}@MIL-117$ ,

was introduced into 10 mL of these dye solutions (Fig. S6†). The mixtures were then thoroughly stirred to ensure adequate interaction between the dye molecules and the adsorbent. After a set contact time, the mixtures were centrifuged to sep-

arate the adsorbent from the supernatant, which contained any unadsorbed dye. To quantify the residual MB dye concentration in the supernatant post-adsorption, UV-visible spectroscopy was used (Fig. 9(a)). This method allowed for precise

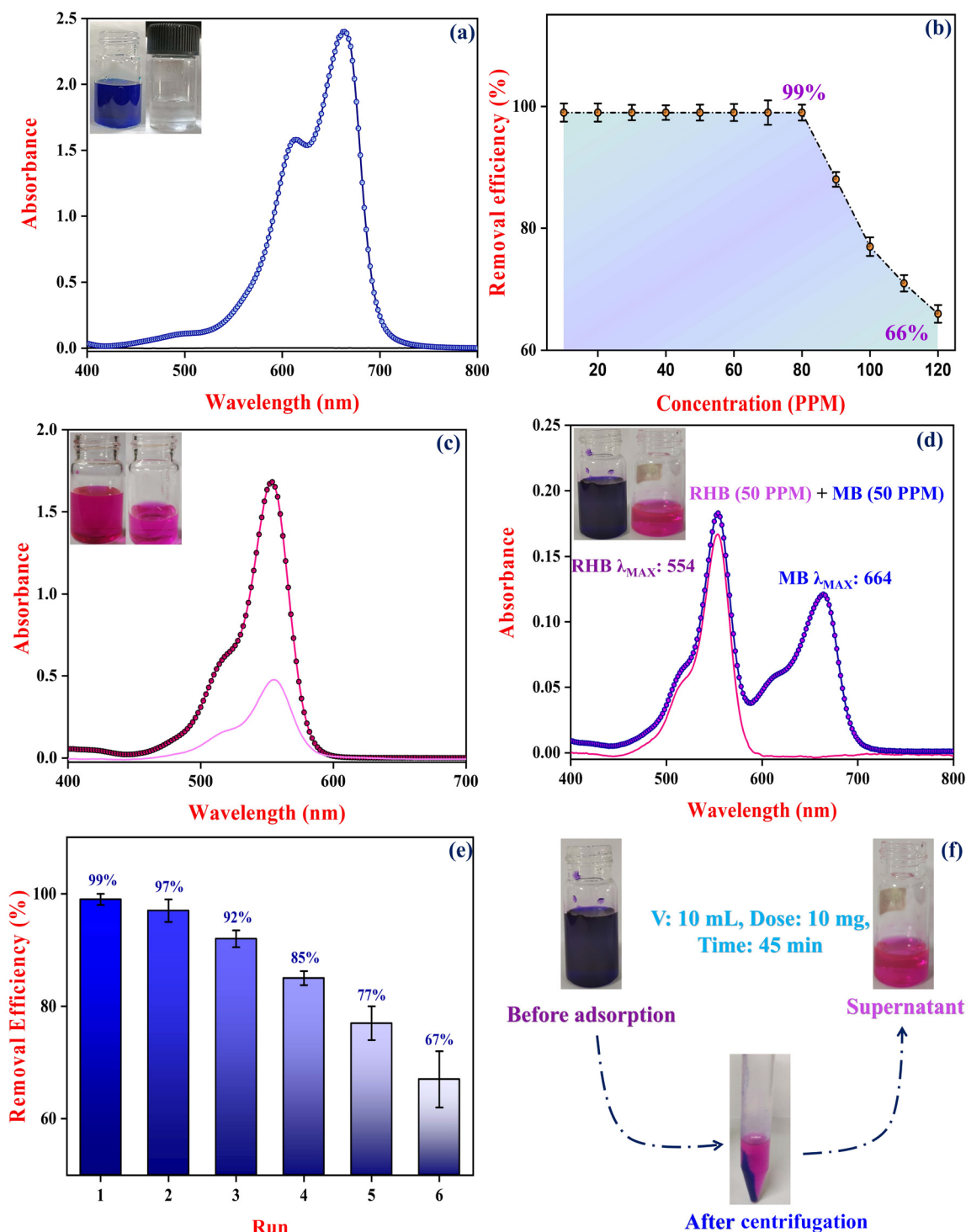


**Fig. 9** (a) UV-vis spectra of MB (80 ppm, 10 mL) removal using  $\text{Mo}_8\text{O}_{26}@MIL-117$  before and after treatment. (b)  $\text{Mo}_8\text{O}_{26}@MIL-117$  removal efficiency for MB solutions ranging from 10 to 120 ppm. (c) UV-vis spectra of RHB (50 ppm, 10 mL) removal using  $\text{Mo}_8\text{O}_{26}@MIL-117$  before and after treatment. (d) Selective dye removal in a MB (50 ppm) and RHB (50 ppm) mixture using  $\text{Mo}_8\text{O}_{26}@MIL-117$ . (e) Reusability cycle of MB over  $\text{Mo}_8\text{O}_{26}@MIL-117$  (80 ppm). (f) Photo of selective filtration of MB over RHB using  $\text{Mo}_8\text{O}_{26}@MIL-117$ .



measurement of the reduction in dye concentration compared to the initial levels. These findings reveal a notable difference in performance between the MIL-117 framework and the  $\text{Mo}_8\text{O}_{26}@MIL-117$  composite, underscoring the advantages of incorporating  $\text{Mo}_8\text{O}_{26}^{4-}$  anions into the MIL-117 structure. The incorporation of  $\text{Mo}_8\text{O}_{26}^{4-}$  anions significantly enhances the surface charge of the  $\text{Mo}_8\text{O}_{26}@MIL-117$  composite. The zeta potential measurement for the composite with a 2 mmol loading of  $\text{Mo}_8\text{O}_{26}^{4-}$  is  $-60.3$  mV, indicating a highly negative surface charge (Fig. S7†). This highly negative charge enhances electrostatic interactions with positively charged MB molecules, thereby promoting adsorption. In contrast, the composite with a lower  $\text{Mo}_8\text{O}_{26}^{4-}$  loading (1 mmol) exhibits a zeta potential of  $-30.4$  mV. The  $\text{Mo}_8\text{O}_{26}@MIL-117$  (2 mmol) composite achieves an impressive 99% dye removal efficiency for 80 ppm. In comparison, the parent MIL-117 framework also attains 99% removal efficiency for MB, but only at concentrations up to 50 ppm (Fig. S8(a)†). The  $\text{Mo}_8\text{O}_{26}@MIL-117$  composite, however, demonstrates superior performance by maintaining this high efficiency even at elevated dye concentrations of up to 80 ppm. This ability to effectively adsorb MB at higher concentrations highlights the significant enhancement in adsorption capacity provided by the incorporation of  $\text{Mo}_8\text{O}_{26}^{4-}$  anions. To assess the adsorption of RHB, 10 milligrams of each adsorbent, MIL-117 and the  $\text{Mo}_8\text{O}_{26}@MIL-117$  composite, were tested in 10 mL of a 50 ppm RHB dye solution. The results showed that MIL-117 removed 52% of RHB within 45 minutes (Fig. S8(c)†), whereas the  $\text{Mo}_8\text{O}_{26}@MIL-117$  composite achieved an enhanced removal efficiency of 72% in the same duration (Fig. 9(c)). This study highlights the significant advantages of incorporating  $\text{Mo}_8\text{O}_{26}^{4-}$  anions into MIL-117 structures for MB and RHB removal.

**2.4.1 Selective dye removal ( $\text{MB}^+/\text{RHB}^+$ ).** Selective dye removal is highly efficient for isolating specific dyes from complicated mixtures.<sup>63</sup> POM@MOF with great selectivity towards the target dye enables the precise removal of the dye while leaving other components untouched. It takes less time and is low cost compared to well-known dye removal methods such as degradation,<sup>64</sup> coagulation,<sup>65</sup> *etc.*, which makes it a more sustainable and environmentally friendly alternative. In the  $\text{MB}^+/\text{RHB}^+$  dye system, both dyes are cationic at concentrations of 50 ppm in a 10 mL volume with an adsorption duration of 45 minutes; the  $\text{Mo}_8\text{O}_{26}@MIL-117$  composite and MIL-117 exhibit remarkable selectivity for MB adsorption. Both MIL-117 and the  $\text{Mo}_8\text{O}_{26}@MIL-117$  composite demonstrated selective removal of MB from a mixture of dyes, showcasing their strong affinity for MB (Fig. S9(d)†). Selective adsorption of cationic dyes is difficult to accomplish, yet these materials show potential in this area. Fig. 9(d) depicts the initial solution state after 45 minutes, revealing the effective adsorption of MB by the composite, as evident from the composite turning blue. The supernatant retains a dark pink colour, indicating the presence of unabsorbed RHB. This selectivity is further confirmed through UV-vis analysis (Fig. 9(f)), corroborating the preferential adsorption of MB by the composite while leaving RHB largely unabsorbed.

## 2.5 Effect of pH, salts, and solvent on MB adsorption onto $\text{Mo}_8\text{O}_{26}@MIL-117$

The influence of pH, salts, and solvent on MB adsorption by the  $\text{Mo}_8\text{O}_{26}@MIL-117$  composite was systematically investigated using a batch adsorption process (MB: 80 ppm,  $\text{Mo}_8\text{O}_{26}@MIL-117$ : 10 mg, and V: 10 mL).

**2.5.1 pH.** The pH of the aqueous solution is a critical variable in the adsorption process, significantly influencing the performance of the  $\text{Mo}_8\text{O}_{26}@MIL-117$  composite in MB removal. The composite exhibits a negative surface charge, which impacts its pH dependent behavior. Under acidic conditions (pH 2–5), the surface charge of the composite becomes less negative due to protonation, which weakens the electrostatic attraction between the composite and MB (Fig. 10(a)). This change can destabilize the structure of the composite, resulting in reduced removal efficiency. At neutral pH (6–7), the composite retains its negative charge, facilitating optimal MB adsorption through strong electrostatic interactions and maintaining structural integrity. The increasing negative charge further supports MB removal under moderately basic conditions (pH 8–10). However, at very high pH levels (>12), the presence of competing hydroxide ions may hinder the adsorption performance. Overall, the  $\text{Mo}_8\text{O}_{26}@MIL-117$  composite exhibits optimal performance in neutral to slightly basic environments (pH 6–8). In contrast, acidic or highly basic conditions are likely to diminish its adsorption capabilities. This understanding of the pH-dependent behavior of the composite provides valuable insights for optimizing adsorption processes in practical applications.

**2.5.2 Salts.** Understanding the influence of various metal ions on the removal efficiency of MB from solution provides valuable insight into the practical performance of  $\text{Mo}_8\text{O}_{26}@MIL-117$  in wastewater treatment. By assessing the impact of monovalent, divalent, and trivalent ions common in real-world wastewater streams, the study offers a comprehensive perspective on the competitive adsorption dynamics that can influence MB removal. Also, the same batch adsorption process was employed, with the addition of an 80 ppm salt solution. This concentration was chosen to match the MB concentration, ensuring equal molar conditions for evaluating the competitive effects of various metal ions on MB removal efficiency. Monovalent ions, such as  $\text{Na}^+$ ,  $\text{K}^+$ , and  $\text{NO}_3^-$ , show the highest removal efficiency, nearly 99% (Fig. 10(b)), due to their low charge density and minimal competition for adsorption sites.  $\text{Mo}_8\text{O}_{26}@MIL-117$  maintains strong electrostatic interactions with MB in their presence. Divalent ions, including  $\text{Ca}^{2+}$ ,  $\text{Mg}^{2+}$ , and  $\text{Ba}^{2+}$ , gradually decrease removal efficiency (95%–90%). Their higher charge density introduces more competition for adsorption sites and increased ionic shielding, weakening the MB and  $\text{Mo}_8\text{O}_{26}@MIL-117$  interaction. The largest decline in MB removal occurs with trivalent ions like  $\text{Al}^{3+}$  and  $\text{Fe}^{3+}$ , where efficiency drops to 85%–80%. These ions create stronger competition for adsorption sites and more pronounced ionic shielding. Additionally,  $\text{Fe}^{3+}$  may form precipitates that block adsorption sites, further reducing MB uptake.

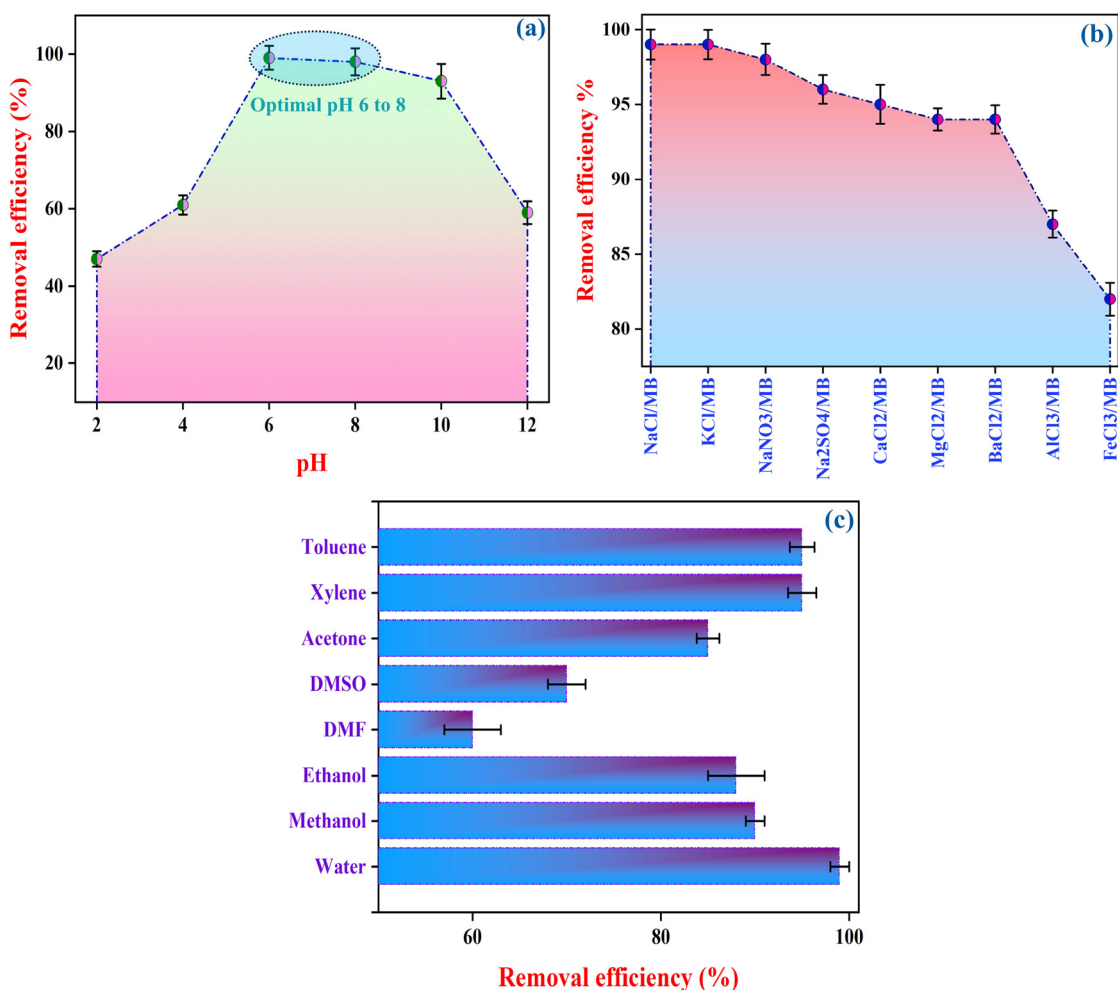


**Fig. 10** (a) Influence of pH (2 to 12) on the MB removal efficiency of  $\text{Mo}_8\text{O}_{26}@MIL-117$ . (b) Impact of different salts on MB adsorption performance. (c) Effect of various solvents on the MB removal efficiency of the  $\text{Mo}_8\text{O}_{26}@MIL-117$  composite.

This study underscores the critical role of ionic strength and charge density in determining the effectiveness of MB adsorption, particularly when transitioning from monovalent to multivalent ions. Understanding these effects helps optimize adsorbent performance in wastewater treatment systems.

**2.5.3 Solvents.** The  $\text{Mo}_8\text{O}_{26}@MIL-117$  composite exhibits excellent dye removal efficiency for MB across a range of solvents, with water showing the highest efficiency at 99% (Fig. 10(c)). This result can be attributed to the strong electrostatic interactions between the negatively charged  $\text{Mo}_8\text{O}_{26}^{4-}$  anions and the cationic MB in a highly polar medium like water. In non-polar solvents such as xylene and toluene, the removal rates are similarly high at 95%. In these environments, the absence of significant solvent-dye interactions reduces competition for adsorption sites on the composite, allowing MB to adsorb effectively onto the  $\text{Mo}_8\text{O}_{26}^{4-}$  anions. In polar protic solvents like methanol and ethanol, the dye removal efficiencies drop slightly to 90% and 88%, respectively. The ability of these solvents to form hydrogen bonds with MB leads to stronger solvent-solute interactions, reducing

the availability of MB for adsorption onto the composite. These competing solvent interactions limit the overall efficiency, though the composite still performs well. For acetone, a polar aprotic solvent, the efficiency remains relatively high at 85%. Acetone does not engage in hydrogen bonding with MB, but its moderate dipole interactions still affect solvation, allowing decent adsorption efficiency. In contrast, more polar aprotic solvents like DMF (60%) and DMSO (71%) show lower removal efficiencies. In these solvents, MB is highly solvated due to their strong polarity, and the solvation shells around MB reduce their availability to interact with the composite's adsorption sites. This demonstrates that strong solvent-solute interactions can significantly hinder the adsorption of MB in these media. Overall, these results highlight the versatility of the  $\text{Mo}_8\text{O}_{26}@MIL-117$  composite, with solvent polarity and solvation effects playing critical roles in the observed dye removal efficiencies. The balance between solvent-dye and solvent-adsorbent interactions is a key factor in determining performance across different solvents.

## 2.6 Kinetics and thermodynamics of MB adsorption onto $\text{Mo}_8\text{O}_{26}@MIL-117$

**2.6.1 Adsorption kinetics.** Kinetic studies were performed to elucidate the adsorption mechanism and rate of MB adsorption onto the  $\text{Mo}_8\text{O}_{26}@MIL-117$  composite, considering the effect of contact time between the liquid phase and the solid surface. The adsorption process involves solute exchange between the liquid and solid phases through mass transfer, prompting the application of both pseudo-first-order (PFO) and pseudo-second-order (PSO) models to fit experimental data obtained at varying contact times. The kinetic analysis revealed that the PSO model provided a superior fit to the data, as evidenced by a higher correlation coefficient ( $R^2 = 0.99$ ; Table S14†), compared to the PFO model ( $R^2 = 0.84$ ). For the PFO model, the rate constant ( $k_1$ ) was determined to be  $4.5 \times 10^{-3} \text{ min}^{-1}$ , with a calculated equilibrium adsorption capacity ( $q_e$ ) of  $85.64 \text{ mg g}^{-1}$ . In contrast, the PSO model yielded a rate constant ( $k_2$ ) of  $3.44 \times 10^{-3} \text{ g mg}^{-1} \text{ min}^{-1}$  and a  $q_e$  value of  $80.67 \text{ mg g}^{-1}$ , which closely aligned with the experimental data (Fig. 11(a)). These results strongly suggest that the adsorption process is predominantly chemisorptive in nature, with the rate-limiting step likely involving electron exchange between the MB molecules and the  $\text{Mo}_8\text{O}_{26}@MIL-117$  composite surface. The high  $R^2$  value for the PSO model underscores its greater accuracy in predicting the adsorption behavior, confirming that this model more effectively captures the kinetics of MB adsorption onto the composite.

**2.6.2 Adsorption thermodynamics.** A systematic investigation into the feasibility, spontaneity, and thermodynamic profile of MB adsorption by the  $\text{Mo}_8\text{O}_{26}@MIL-117$  composite was conducted through a series of controlled experiments. The experiments were conducted at different temperatures (30 °C, 40 °C, 50 °C, and 60 °C) while keeping all other parameters constant:  $\text{Mo}_8\text{O}_{26}@MIL-117$  (10 mg), solution volume (10 mL), and MB concentration (80 ppm). This experimental framework enabled a detailed analysis of the adsorption process, offering

critical insights into the governing thermodynamic mechanisms. Negative Gibbs free energy values ( $\Delta G^\circ$ ) across all temperatures confirm that the adsorption process is spontaneous. At 303 K,  $\Delta G^\circ$  was  $-9.54 \text{ kJ mol}^{-1}$ , and it became more negative with increasing temperature, reaching  $-12.82 \text{ kJ mol}^{-1}$  at 333 K (Table S15†), indicating that adsorption is more favorable at higher temperatures and suggesting an endothermic process. The values of  $\Delta S^\circ$  and  $\Delta H^\circ$  were derived from the intercept and slope of the linear plot of  $\ln k$  vs.  $1/T$  (Fig. 11(b)). The enthalpy change ( $\Delta H = 23.94 \text{ kJ mol}^{-1}$ ) suggests chemisorption, as this value is typically associated with the energy range for chemical adsorption, indicating the formation of bonds between the adsorbate and adsorbent. The positive entropy change ( $\Delta S^\circ = 110.46 \text{ J mol}^{-1} \text{ K}^{-1}$ ) reflects increased randomness at the solid-liquid interface, likely due to the displacement of water molecules and a less ordered arrangement of MB molecules on the composite. Collectively, these thermodynamic findings indicate that MB adsorption onto  $\text{Mo}_8\text{O}_{26}@MIL-117$  is spontaneous, endothermic, and predominantly chemisorptive, involving strong interactions between the dye molecules and the composite material.

## 2.7 Adsorbent stability

The stability of the composite material in water is important, particularly considering the toxicity of indium (In)<sup>66</sup> and molybdenum (Mo)<sup>67</sup> to aquatic ecosystems. Prolonged exposure of these elements to water bodies can harm flora and fauna. In this study, the composite was immersed in water and stirred for 72 hours to evaluate its stability. Following the stirring process, the supernatant was separated by centrifugation and analysed using ICP-OES to detect any leaching of Mo and In (Fig. S10†). The results revealed no Mo and In leaching (Table S16†). Furthermore, the MIL-117 component exhibited remarkable water stability, with negligible signs of degradation or leaching for 72 hours. This finding underscores the resilience of the MIL-117 component in aquatic environments,

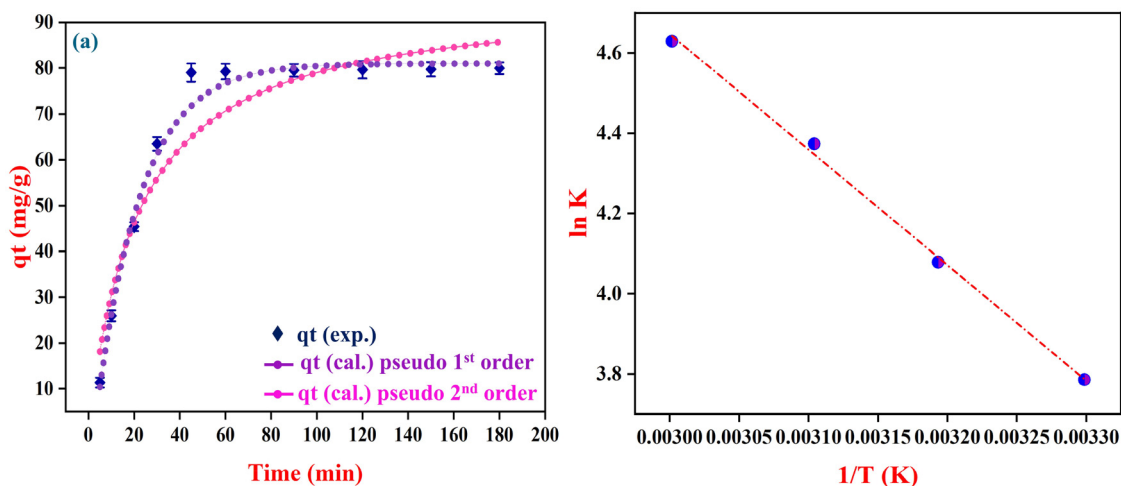
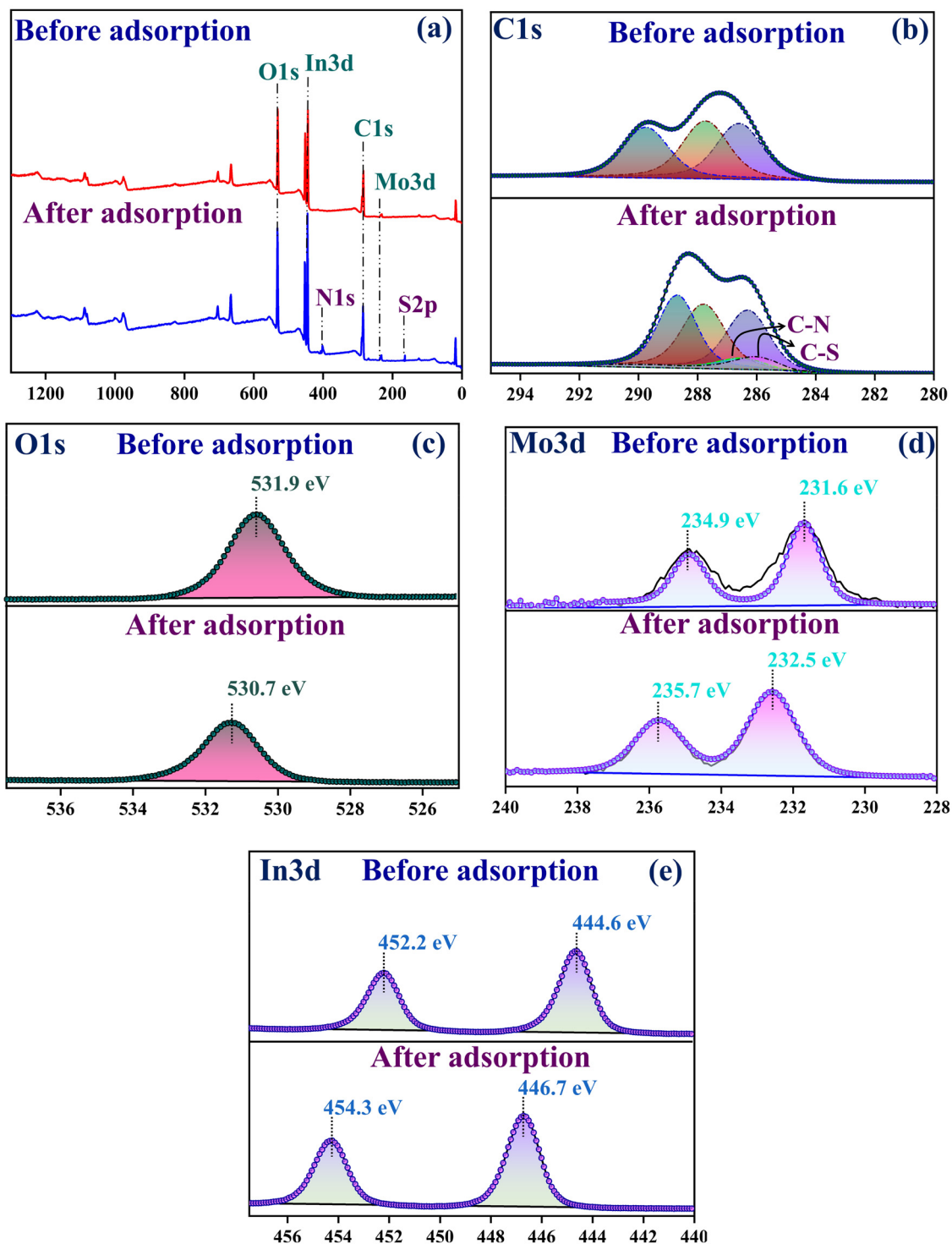


Fig. 11 (a) Pseudo-first and second-order kinetic plots. (b) Thermodynamic linear fitting for the adsorption of MB onto the  $\text{Mo}_8\text{O}_{26}@MIL-117$  composite.

making it highly suitable for applications in wastewater treatment where high-water stability and minimal ion leaching are crucial. This stability is critical to prevent the release of toxic metals into water systems, thereby safeguarding environmental health.

## 2.8 Adsorbent reusability

The reusability of the  $\text{Mo}_8\text{O}_{26}@MIL-117$  composite was rigorously evaluated by examining its ability to remove MB (10 mL, 80 PPM) dye over multiple cycles. After each adsorption cycle,



**Fig. 12** High-resolution XPS spectra before and after filtration of MB over  $\text{Mo}_8\text{O}_{26}@MIL-117$ : (a) survey scan; (b) C 1s, (c) O 1s, (d) Mo 3d and (e) In 3d. (X-axis: binding energy (eV); Y-axis: intensity (a.u.)).



desorption of MB was performed using 0.2 M NaOH. The composite was then recovered through centrifugation and reactivated under vacuum at 100 °C (Fig. S11†). This process was repeated across five cycles to determine the durability and efficiency of the composite in reusability scenarios. Initially, the Mo<sub>8</sub>O<sub>26</sub>@MIL-117 composite exhibited a high removal efficiency of 99% in the first cycle. Remarkably, its performance decreased in efficiency, reaching 67% by the sixth cycle (Fig. 9(e), S9, and S10†). Such good performance over multiple cycles underscores the composite's strength and highlights its potential for sustained use in adsorption processes. Even after several cycles, the observed high removal efficiencies indicate that the Mo<sub>8</sub>O<sub>26</sub>@MIL-117 composite is well-suited for repeated applications in wastewater treatment and other scenarios where effective reusability is critical.

### 2.9 Adsorbent dye removal mechanism

The removal mechanism of MB by Mo<sub>8</sub>O<sub>26</sub>@MIL-117 has been investigated using XPS. Mo<sub>8</sub>O<sub>26</sub>@MIL-117 follows a similar adsorption behaviour to the MIL-117 solid in batch adsorption processes. The MB removal mechanism involves several robust potential pathways. One plausible explanation is the pivotal role played by electrostatic interactions between the cationic dyes MB and the MIL-117 and Mo<sub>8</sub>O<sub>26</sub><sup>4-</sup> within the structure. Additionally, other interactions, such as hydrogen bonding and  $\pi$ - $\pi$  stacking between the benzene ring of MIL-117 and the dye molecules, cannot be disregarded. The overall adsorption mechanism is intricate, demanding a more comprehensive understanding of the interaction between MB and Mo<sub>8</sub>O<sub>26</sub>@MIL-117. The XPS survey scan verified the presence of a sulphur 2p peak, indicating the presence of MB (Fig. 12(a)). The high-resolution C 1s spectra of Mo<sub>8</sub>O<sub>26</sub>@MIL-117 obtained before and after MB adsorption exhibit the same three peaks at 286.3 eV, 287.8 eV, and 288.8 eV BEs, corresponding to C-O, C=O, and O-C=O, respectively. In the spectra obtained after adsorption, two additional peaks appear at 286.5 eV and 286.0 eV, indicating the presence of C-S and C-N bonds of MB (Fig. 12(b)). The observed slight increase in BE is likely attributed to alterations in the chemical environment stemming from the adsorption of MB onto the tubular channels of the composite. The XPS spectra for both O 1s (Fig. 12(c)) and Mo 3d (Fig. 12(d)), obtained before and after adsorption, show distinctive peaks at varying BEs. Before adsorption, the XPS analysis of Mo<sub>8</sub>O<sub>26</sub>@MIL-117 reveals the O 1s peak at 530.6 eV. However, after the adsorption of MB, this peak shifts to 531.3 eV. Similarly, the Mo 3d peaks, initially at 531.6 eV and 534.9 eV, shift to 532.5 eV and 535.7 eV after adsorption. These slight shifts in BEs suggest that oxygen and molybdenum interact with MB molecules. The changes indicate a reduction in electron density and modifications in the chemical environment within the tubular channels of the composite, facilitating the adsorption process. Also, the XPS data for In 3d reveal a shift in BEs from 444.6 eV and 452.2 eV to 446.7 eV and 454.3 (Fig. 12(e)), indicative of a change in the chemical environment and a reduction in electron density from the indium nucleus due to interactions with guest molecules.

## 3. Conclusion

A polyoxometalate-loaded MOF composite material, *i.e.* Mo<sub>8</sub>O<sub>26</sub>@MIL-117, has been developed successfully *via* an encapsulation method and a systematic study on its structural and chemical properties has been done. The confirmation of Mo<sub>8</sub>O<sub>26</sub><sup>4-</sup> anion encapsulation within MIL-117 tubular channels was attained through various spectral techniques and analytical methods like FTIR, XRD, FE-SEM, N<sub>2</sub> adsorption-desorption isotherms, EDX, XPS, and TGA. The analyses collectively confirmed the integrity of the MIL-117 framework post-encapsulation, highlighting the effective trapping of Mo<sub>8</sub>O<sub>26</sub><sup>4-</sup> anions. Furthermore, Mo<sub>8</sub>O<sub>26</sub>@MIL-117 demonstrated efficient catalytic activity in oxidative C-N bond formation and Paal-Knorr pyrrole synthesis across diverse substrates, including aromatic and sterically hindered amines, yielding excellent product yields. The catalyst exhibited robust stability and recyclability over multiple cycles. The Mo<sub>8</sub>O<sub>26</sub>@MIL-117 composite significantly improves dye removal efficiency, particularly for MB, demonstrating higher capacity, stability, and reusability compared to MIL-117 alone. Its selective adsorption for MB over RHB, minimal Mo<sub>8</sub>O<sub>26</sub><sup>4-</sup> leaching, and robust performance over multiple cycles make it a promising material for sustainable and efficient wastewater treatment applications. Detailed XPS of the composite after MB adsorption elucidated intricate changes in chemical environments upon MB adsorption, revealing the formation of C-S and C-N bonds. These insights deepen our understanding of MB adsorption mechanisms within the tubular channels of the composite material, reinforcing its efficacy in environmental remediation contexts.

## Author contributions

K. M. meticulously researched and crafted the comprehensive draft. Additionally, R. J. and S. K. provided guidance as mentors, offering their expertise and granting final approval for the manuscript's final version.

## Data availability

The data supporting this article have been included as part of the ESI.†

## Conflicts of interest

There are no conflicts to declare.

## Acknowledgements

R. J. thanks Gujarat Council on Science & Technology (Project No. GUJCOST/STI/2021-22/3877) for providing financial support. K. M. is thankful to the SVNIT Surat for providing a

fellowship for his research work. We also extend our gratitude and acknowledge M.Sc. dissertation student, Mr Amarendra Singh for assisting in catalytic work.

## References

- O. M. Yaghi, M. O'Keeffe, N. W. Ockwig, H. K. Chae, M. Eddaoudi and J. Kim, Reticular synthesis and the design of new materials, *Nature*, 2003, **423**(6941), 705–714.
- D. J. Tranchemontagne, J. L. Mendoza-Cortés, M. O'Keeffe and O. M. Yaghi, Secondary building units, nets and bonding in the chemistry of metal–organic frameworks, *Chem. Soc. Rev.*, 2009, **38**(5), 1257–1283, DOI: [10.1039/B817735J](https://doi.org/10.1039/B817735J).
- L. Yan, H.-T. Zheng, L. Song, Z.-W. Wei, J.-J. Jiang and C.-Y. Su, Microporous Fluorinated MOF with Multiple Adsorption Sites for Efficient Recovery of C<sub>2</sub>H<sub>6</sub> and C<sub>3</sub>H<sub>8</sub> from Natural Gas, *ACS Appl. Mater. Interfaces*, 2024, **16**(5), 6579–6588.
- K. Maru, S. Kalla and R. Jangir, Efficient Dye Extraction from Wastewater Using Indium-MOF-Immobilized Polyvinylidene Fluoride Membranes with Selective Filtration for Enhanced Remediation, *Langmuir*, 2024, **40**(15), 8144–8161.
- K. Maru, S. Kalla and R. Jangir, MOF/POM hybrids as catalysts for organic transformations, *Dalton Trans.*, 2022, **51**(32), 11952–11986.
- J. Juan-Alcañiz, E. V. Ramos-Fernandez, U. Lafont, J. Gascon and F. Kapteijn, Building MOF bottles around phosphotungstic acid ships: One-pot synthesis of bi-functional polyoxometalate-MIL-101 catalysts, *J. Catal.*, 2010, **269**(1), 229–241.
- C. Xiao, X. Guo and J. Li, From nano- to macroarchitectures: designing and constructing MOF-derived porous materials for persulfate-based advanced oxidation processes, *Chem. Commun.*, 2024, **60**(33), 4395–4418.
- L. Nie, Y. Yang, C. Fang, H. Chen and S. Xin, Co-doped metal–organic framework MIL-125(Ti) derivate for efficient adsorption of tetracycline hydrochloride from water, *Appl. Surf. Sci.*, 2023, **640**, 158390.
- G. Cai, P. Yan, L. Zhang, H.-C. Zhou and H.-L. Jiang, Metal–Organic Framework-Based Hierarchically Porous Materials: Synthesis and Applications, *Chem. Rev.*, 2021, **121**(20), 12278–12326.
- E. M. Abd El-Monaem, A. S. Eltaweil, G. M. El-Subruiti, M. S. Mohy-Eldin and A. M. Omer, Adsorption of nitrophenol onto a novel Fe<sub>3</sub>O<sub>4</sub>-κ-carrageenan/MIL-125(Ti) composite: process optimization, isotherms, kinetics, and mechanism, *Environ. Sci. Pollut. Res.*, 2023, **30**(17), 49301–49313.
- Q. Hu, J. Dong, Y. Chen, J. Yi, J. Xia, S. Yin and H. Li, *In situ* construction of bifunctional MIL-125(Ti)/BiOI reactive adsorbent/photocatalyst with enhanced removal efficiency of organic contaminants, *Appl. Surf. Sci.*, 2022, **583**, 152423.
- M. R. Horn, A. Singh, S. Alomari, S. Goberna-Ferrón, R. Benages-Vilau, N. Chodankar, N. Motta, K. Ostrikov, J. MacLeod, P. Sonar, *et al.*, Polyoxometalates (POMs): from electroactive clusters to energy materials, *Energy Environ. Sci.*, 2021, **14**(4), 1652–1700.
- Y. Zhang, Y. Li, H. Guo, Y. Guo and R. Song, Recent advances in polyoxometalate-based materials and their derivatives for electrocatalysis and energy storage, *Mater. Chem. Front.*, 2024, **8**(3), 732–768.
- L. Vilà-Nadal and L. Cronin, Design and synthesis of polyoxometalate-framework materials from cluster precursors, *Nat. Rev. Mater.*, 2017, **2**(10), 17054.
- H. N. Miras, L. Vilà-Nadal and L. Cronin, Polyoxometalate based open-frameworks (POM-OFs), *Chem. Soc. Rev.*, 2014, **43**(16), 5679–5699.
- X. López, J. J. Carbó, C. Bo and J. M. Poblet, Structure, properties and reactivity of polyoxometalates: a theoretical perspective, *Chem. Soc. Rev.*, 2012, **41**(22), 7537–7571.
- V. I. Parvulescu and H. García, Heterogeneous catalysis based on supramolecular association, *Catal. Sci. Technol.*, 2018, **8**(19), 4834–4857.
- X. Zhong, Y. Lu, F. Luo, Y. Liu, X. Li and S. Liu, A Nanocrystalline POM@MOFs Catalyst for the Degradation of Phenol: Effective Cooperative Catalysis by Metal Nodes and POM Guests, *Chem. – Eur. J.*, 2018, **24**(12), 3045–3051.
- G. Paille, M. Gomez-Mingot, C. Roch-Marchal, M. Haouas, Y. Benseghir, T. Pino, M.-H. Ha-Thi, G. Landrot, P. Mialane, M. Fontecave, *et al.*, Thin Films of Fully Noble Metal-Free POM@MOF for Photocatalytic Water Oxidation, *ACS Appl. Mater. Interfaces*, 2019, **11**(51), 47837–47845.
- N. V. Maksimchuk, K. A. Kovalenko, S. S. Arzumanov, Y. A. Chesalov, M. S. Melgunov, A. G. Stepanov, V. P. Fedin and O. A. Kholdeeva, Hybrid Polyoxotungstate/MIL-101 Materials: Synthesis, Characterization, and Catalysis of H<sub>2</sub>O<sub>2</sub>-Based Alkene Epoxidation, *Inorg. Chem.*, 2010, **49**(6), 2920–2930.
- Q. Han, L. Zhang, C. He, J. Niu and C. Duan, Metal–Organic Frameworks with Phosphotungstate Incorporated for Hydrolytic Cleavage of a DNA-Model Phosphodiester, *Inorg. Chem.*, 2012, **51**(9), 5118–5127.
- X. Tian, L. Hou, J. Wang, X. Xin, H. Zhang, Y. Ma, Y. Wang, L. Zhang and Z. Han, Novel fully reduced phosphomolybdates for highly efficient removal of inorganic hexavalent chromium and the organic dye methylene blue, *Dalton Trans.*, 2018, **47**(42), 15121–15130.
- S. Zhang, F. Ou, S. Ning and P. Cheng, Polyoxometalate-based metal–organic frameworks for heterogeneous catalysis, *Inorg. Chem. Front.*, 2021, **8**(7), 1865–1899.
- Y. Liu, C. Tang, M. Cheng, M. Chen, S. Chen, L. Lei, Y. Chen, H. Yi, Y. Fu and L. Li, Polyoxometalate@Metal–Organic Framework Composites as Effective Photocatalysts, *ACS Catal.*, 2021, **11**(21), 13374–13396.
- N. Aramesh, A. Reza Bagheri, Z. Zhang, B. Yadollahi and H. Kee Lee, Polyoxometalate-based materials against environmental pollutants: A review, *Coord. Chem. Rev.*, 2024, **507**, 215767.

- 26 A. S. Cherevan, S. P. Nandan, I. Roger, R. Liu, C. Streb and D. Eder, Polyoxometalates on Functional Substrates: Concepts, Synergies, and Future Perspectives, *Adv. Sci.*, 2020, **7**(8), 1903511.
- 27 B. J. S. Johnson and A. Stein, Surface Modification of Mesoporous, Macroporous, and Amorphous Silica with Catalytically Active Polyoxometalate Clusters, *Inorg. Chem.*, 2001, **40**(4), 801–808.
- 28 W. Qi and L. Wu, Polyoxometalate/polymer hybrid materials: fabrication and properties, *Polym. Int.*, 2009, **58**(11), 1217–1225.
- 29 R. Xue, Y.-S. Liu, M.-Y. Wang, H. Guo, W. Yang and G.-Y. Yang, Combination of covalent organic frameworks (COFs) and polyoxometalates (POMs): the preparation strategy and potential application of COF–POM hybrids, *Mater. Horiz.*, 2023, **10**(11), 4710–4723.
- 30 M. Lu, M. Zhang, J. Liu, T.-Y. Yu, J.-N. Chang, L.-J. Shang, S.-L. Li and Y.-Q. Lan, Confining and Highly Dispersing Single Polyoxometalate Clusters in Covalent Organic Frameworks by Covalent Linkages for CO<sub>2</sub> Photoreduction, *J. Am. Chem. Soc.*, 2022, **144**(4), 1861–1871.
- 31 X. Luo, F. Li, F. Peng, L. Huang, X. Lang and M. Shi, Strategies for Perfect Confinement of POM@MOF and Its Applications in Producing Defect-Rich Electrocatalyst, *ACS Appl. Mater. Interfaces*, 2021, **13**(48), 57803–57813.
- 32 X. Li, L. Yang, Q. Liu, W. Bai, H. Li, M. Wang, Q. Qian, Q. Yang, C. Xiao and Y. Xie, Directional Shunting of Photogenerated Carriers in POM@MOF for Promoting Nitrogen Adsorption and Oxidation, *Adv. Mater.*, 2023, **35**(44), 2304532.
- 33 T. Islamoglu, S. Goswami, Z. Li, A. J. Howarth, O. K. Farha and J. T. Hupp, Postsynthetic Tuning of Metal–Organic Frameworks for Targeted Applications, *Acc. Chem. Res.*, 2017, **50**(4), 805–813.
- 34 K.-Y. Wang, J. Zhang, Y.-C. Hsu, H. Lin, Z. Han, J. Pang, Z. Yang, R.-R. Liang, W. Shi and H.-C. Zhou, Bioinspired Framework Catalysts: From Enzyme Immobilization to Biomimetic Catalysis, *Chem. Rev.*, 2023, **123**(9), 5347–5420.
- 35 C. T. Buru and O. K. Farha, Strategies for Incorporating Catalytically Active Polyoxometalates in Metal–Organic Frameworks for Organic Transformations, *ACS Appl. Mater. Interfaces*, 2020, **12**(5), 5345–5360.
- 36 M. Samaniyan, M. Mirzaei, R. Khajavian, H. Eshtiagh-Hosseini and C. Streb, Heterogeneous Catalysis by Polyoxometalates in Metal–Organic Frameworks, *ACS Catal.*, 2019, **9**(11), 10174–10191.
- 37 Q. An, Z. Xu, W. Shang, Y. Wang, X. Liu, D. Guo, M. Zeng and Z. Jia, Polyoxometalate-Based Metal–Organic Frameworks as the Solid Support to Immobilize MP-11 Enzyme for Enhancing Thermal and Recyclable Stability, *ACS Appl. Bio Mater.*, 2022, **5**(3), 1222–1229.
- 38 B. D’Cruz, M. O. Amin and E. Al-Hetlani, Polyoxometalate-Based Materials for the Removal of Contaminants from Wastewater: A Review, *Ind. Eng. Chem. Res.*, 2021, **60**(30), 10960–10977.
- 39 G. Férey, C. Mellot-Draznieks, C. Serre, F. Millange, J. Dutour, S. Surblé and I. Margiolaki, A Chromium Terephthalate-Based Solid with Unusually Large Pore Volumes and Surface Area, *Science*, 2005, **309**(5743), 2040–2042.
- 40 P. Mialane, C. Mellot-Draznieks, P. Gairola, M. Duguet, Y. Benseghir, O. Oms and A. Dolbecq, Heterogenisation of polyoxometalates and other metal-based complexes in metal–organic frameworks: from synthesis to characterisation and applications in catalysis, *Chem. Soc. Rev.*, 2021, **50**(10), 6152–6220.
- 41 X.-S. Wang, L. Li, J. Liang, Y.-B. Huang and R. Cao, Boosting Oxidative Desulfurization of Model and Real Gasoline over Phosphotungstic Acid Encapsulated in Metal–Organic Frameworks: The Window Size Matters, *ChemCatChem*, 2017, **9**(6), 971–979.
- 42 H. Liu, L.-G. Gong, C.-X. Wang, C.-M. Wang, K. Yu and B.-B. Zhou, {Cu<sub>2</sub>SiW<sub>12</sub>O<sub>40</sub>}@HKUST-1 synthesized by a one-step solution method with efficient bifunctional activity for supercapacitors and the oxygen evolution reaction, *J. Mater. Chem. A*, 2021, **9**(22), 13161–13169.
- 43 Y. Dong, J. Zhang, Y. Yang, L. Qiu, D. Xia, K. Lin, J. Wang, X. Fan and R. Fan, Self-Assembly of Hybrid Oxidant POM@Cu-BTC for Enhanced Efficiency and Long-Term Stability of Perovskite Solar Cells, *Angew. Chem., Int. Ed.*, 2019, **58**(49), 17610–17615.
- 44 B.-H. Wang and B. Yan, Polyoxometalate-based metal–organic framework NENU-5 hybrid materials for photoluminescence tuning by introducing lanthanide ions and their functionalized soft ionogel/thin film, *CrystEngComm*, 2019, **21**(7), 1186–1192.
- 45 C. T. Buru, P. Li, B. L. Mehdi, A. Dohnalkova, A. E. Platero-Prats, N. D. Browning, K. W. Chapman, J. T. Hupp and O. K. Farha, Adsorption of a Catalytically Accessible Polyoxometalate in a Mesoporous Channel-type Metal–Organic Framework, *Chem. Mater.*, 2017, **29**(12), 5174–5181.
- 46 Y. Benseghir, A. Lemarchand, M. Duguet, P. Mialane, M. Gomez-Mingot, C. Roch-Marchal, T. Pino, M.-H. Ha-Thi, M. Haouas, M. Fontecave, *et al.* Co-immobilization of a Rh Catalyst and a Keggin Polyoxometalate in the UiO-67 Zr-Based Metal–Organic Framework: In Depth Structural Characterization and Photocatalytic Properties for CO<sub>2</sub> Reduction, *J. Am. Chem. Soc.*, 2020, **142**(20), 9428–9438.
- 47 L. Bromberg, Y. Diao, H. Wu, S. A. Speakman and T. A. Hatton, Chromium(III) Terephthalate Metal Organic Framework (MIL-101): HF-Free Synthesis, Structure, Polyoxometalate Composites, and Catalytic Properties, *Chem. Mater.*, 2012, **24**(9), 1664–1675.
- 48 S. Bhattacharya, W. W. Ayass, D. H. Taffa, T. Nisar, T. Balster, A. Hartwig, V. Wagner, M. Wark and U. Kortz, Polyoxopalladate-Loaded Metal–Organic Framework (POP@MOF): Synthesis and Heterogeneous Catalysis, *Inorg. Chem.*, 2020, **59**(15), 10512–10521.
- 49 M. Mazaj, C. Volkringer, T. Loiseau, V. Kaučič and G. Férey, Synthesis and crystal structure of a new MOF-type indium

- pyromellitate (MIL-117) with infinite chains of unusual cis connection of octahedra  $\text{InO}_4(\text{OH})_2$ , *Solid State Sci.*, 2011, **13**(8), 1488–1493.
- 50 M. Ayed, S. Thabet and A. Haddad, Crystal Structure and Physicochemical Properties of Two Supramolecular Compounds:  $(\text{C}_4\text{H}_8\text{NH}_2)_4[\text{Mo}_8\text{O}_{26}]$  and  $(\text{NH}_4)_2\text{Na}_2[\text{AsIII}\text{Mo}_6\text{O}_{21}(\text{O}_2\text{CCH}_2\text{NH}_3)_3]\cdot 8\text{H}_2\text{O}$ , *J. Inorg. Organomet. Polym. Mater.*, 2014, **24**(2), 291–301.
- 51 H. Jiang, H. Cheng, C. Zang, J. Tan, B. Sun and F. Bian, Photocatalytic aldehydes/alcohols/toluenes oxidative amidation over bifunctional Pd/MOFs: Effect of Fe-O clusters and Lewis acid sites, *J. Catal.*, 2021, **401**, 279–287.
- 52 S. Jamalifard, J. Mokhtari and Z. Mirjafary, One-pot synthesis of amides via the oxidative amidation of aldehydes and amines catalyzed by a copper-MOF, *RSC Adv.*, 2019, **9**(39), 22749–22754.
- 53 J. Li, J. Jiao, J. Chang, M. Li and Q. Han, Visible-Light-Driven C–N Bond Formation by a Hexanickel Cluster Substituted Polyoxometalate-Based Photocatalyst, *Inorg. Chem.*, 2021, **60**(13), 10022–10029.
- 54 B. Goel, V. Vyas, N. Tripathi, A. Kumar Singh, P. W. Menezes, A. Indra and S. K. Jain, Amidation of Aldehydes with Amines under Mild Conditions Using Metal-Organic Framework Derived  $\text{NiO@Ni}$  Mott-Schottky Catalyst, *ChemCatChem*, 2020, **12**(22), 5743–5749.
- 55 A. Dhakshinamoorthy and H. Garcia, Metal-organic frameworks as solid catalysts for the synthesis of nitrogen-containing heterocycles, *Chem. Soc. Rev.*, 2014, **43**(16), 5750–5765.
- 56 R. Khajuria, S. Dham and K. K. Kapoor, Active methylenes in the synthesis of a pyrrole motif: an imperative structural unit of pharmaceuticals, natural products and optoelectronic materials, *RSC Adv.*, 2016, **6**(43), 37039–37066.
- 57 K. Mezgebe, Y. Melaku and E. Mulugeta, Synthesis and Pharmacological Activities of Chalcone and Its Derivatives Bearing N-Heterocyclic Scaffolds: A Review, *ACS Omega*, 2023, **8**(22), 19194–19211.
- 58 H. Sudibyo, B. Budhijanto, D. V. Cabrera, A. Mahannada, L. Marbelia, D. J. Prasetyo and M. Anwar, Kinetic and Thermodynamic Evidence of the Paal-Knorr and Debus-Radziszewski Reactions Underlying Formation of Pyrroles and Imidazoles in Hydrothermal Liquefaction of Glucose-Glycine Mixtures, *Energy Fuels*, 2024, **38**(4), 3343–3356.
- 59 R. Keshavarz, M. Farahi, B. Karami, P. Gheibipour and A. Zarnegaryan,  $\text{TiO}_2$ -coated graphene oxide-molybdate complex as a new separable nanocatalyst for the synthesis of pyrrole derivatives by Paal-Knorr reaction, *Arabian J. Chem.*, 2022, **15**(5), 103736.
- 60 N. T. S. Phan, T. T. Nguyen, Q. H. Luu and L. T. L. Nguyen, Paal-Knorr reaction catalyzed by metal-organic framework IRMOF-3 as an efficient and reusable heterogeneous catalyst, *J. Mol. Catal. A: Chem.*, 2012, **363–364**, 178–185.
- 61 W. Zhang, M. Kauer, O. Halbherr, K. Epp, P. Guo, M. I. Gonzalez, D. J. Xiao, C. Wiktor, F. X. Liabrés i Xamena, C. Wöll, *et al.* Ruthenium Metal-Organic Frameworks with Different Defect Types: Influence on Porosity, Sorption, and Catalytic Properties, *Chem. – Eur. J.*, 2016, **22**(40), 14297–14307.
- 62 L. Qi, Y. Gong, M. Fang, Z. Jia, N. Cheng and L. Yu, Surface-Active Ionic-Liquid-Encapsulated Polyoxometalate Nanospheres: Construction, Self-Assembly, Adsorption Behavior, and Application for Dye Removal, *ACS Appl. Nano Mater.*, 2020, **3**(1), 375–383.
- 63 X. Zhang, Z. Li, S. Lin and P. Théato, Fibrous Materials Based on Polymeric Salicyl Active Esters as Efficient Adsorbents for Selective Removal of Anionic Dye, *ACS Appl. Mater. Interfaces*, 2020, **12**(18), 21100–21113.
- 64 H. Zhao, Q. Xia, H. Xing, D. Chen and H. Wang, Construction of Pillared-Layer MOF as Efficient Visible-Light Photocatalysts for Aqueous Cr(VI) Reduction and Dye Degradation, *ACS Sustainable Chem. Eng.*, 2017, **5**(5), 4449–4456.
- 65 M. Chethana, L. G. Sorokhaibam, V. M. Bhandari, S. Raja and V. V. Ranade, Green Approach to Dye Wastewater Treatment Using Biocoagulants, *ACS Sustainable Chem. Eng.*, 2016, **4**(5), 2495–2507.
- 66 H.-F. Chang, P.-T. Yang, H.-W. Lin, K.-C. Yeh, M.-N. Chen and S.-L. Wang, Indium Uptake and Accumulation by Rice and Wheat and Health Risk Associated with Their Consumption, *Environ. Sci. Technol.*, 2020, **54**(23), 14946–14954.
- 67 J. Yang, Z. Song, J. Ma and H. Han, Toxicity of Molybdenum-Based Nanomaterials on the Soybean-Rhizobia Symbiotic System: Implications for Nutrition, *ACS Appl. Nano Mater.*, 2020, **3**(6), 5773–5782.